MODELING, FABRICATION, AND CHARACTERIZATION OF POROUS INCONEL 718 STRUCTURES USING SELECTIVE LASER MELTING PROCESS

by

SRIHARI SRIVATHSAN

Presented to the Faculty of the Graduate School of

The University of Texas at Arlington

in partial fulfillment of the requirements

for the degree of

MASTER OF SCIENCE IN MECHANICAL ENGINEERING

THE UNIVERSITY OF TEXAS AT ARLINGTON

May 2020

Acknowledgmen

I would like to show my gratitude to everyone who helped me make this project a success. As with anything of this scale, countless people guided me at various points, all of whom have influenced the process and outcome of this thesis work. However, I would like to thank some people, specifically for their significant contributions and support.

I thank my supervisor, Dr. Amir Ameri, for giving me this excellent opportunity to learn and grow through this thesis project. I am grateful for his constant support during my post-graduation at the University of Texas at Arlington. None of this work would be possible without him.

I owe many thanks to the committee members, Dr. Robert Taylor and Dr. Chen Kan, for making time in their busy schedules to advise, direct, and help drive this research to completion. This work would not be possible without their guidance.

I thank all my colleagues who I had the pleasure of working in the Advanced Materials Engineering Research & Innovation (AMERI) Lab. Without their assistance, it would have been very daunting to complete this work in its entirety.

I also extend my thanks to the Department of Mechanical and Aerospace Engineering, University of Texas, Arlington for administrative support, use of the equipment, and for the provision of courses and literature, which helped me immensely in my journey of personal development.

Last but certainly not least, I would like to express my appreciation for my family, friends, and loved ones, their unwavering support gave me the strength to see this academic pursuit through.

Abstract

MODELING, FABRICATION, AND CHARACTERIZATION OF POROUS INCONEL 718 STRUCTURES USING SELECTIVE LASER MELTING PROCESS

Srihari Srivathsan, M.S

The University of Texas at Arlington, 2020

Supervising Professor: Dr. Amir Ameri

Bio-inspired cellular structures are of great interest these days for many applications, from engineering research to industries. Honeycomb, Body-Centered Cubic with/without Z-struts (BCC-Z/ BCC), Face Centered Cubic with/without Z-struts (FCC-Z/ FCC), and Triply Periodic Minimal Surface (TPMS) such as Gyroid, Diamond, and Schwartz lattices are the most common bio-inspired lattice structures. These structures can be tailored based on their structural organization resulting in superior materials with lightweight properties, adequate strength, and low stiffness. Thankfully, additive manufacturing (AM) has made the fabrication of these complex cellular materials realistic. However, the use of AM could lead to several defects, such as damaged cell walls, irregular thickness, flawed joints, partially missing layers, and improper elastic/plastic behavior. The critical aspect is to try and reduce the manufacturing defects that can help evaluate the overall performance of lattice structures. The primary goal is to discover the characteristics of each morphology type, pore size, porosity percentage by assessing their fabrication quality, microstructure, and mechanical behavior. To these ends, cellular structures of different volume fraction, pore shape, and unit cell size are designed and manufactured using selective laser melting (SLM), the most common AM process. The produced samples are characterized through optical microscopy, scanning electron microscopy (SEM), and x-ray powder diffraction (XRD). Finally, a comprehensive report on optimal porosity design is provided after studying the fundamental parameters from the design, fabrication, and testing phases. The knowledge obtained in this research will enable the production of lightweight metallic devices with custom spatially designed properties by additive manufacturing.

Table of Contents

List of Tables

List of Figures

Chapter 1. Introduction

1.1. Motivation

The third decade of the 21st century has given rise to the use of a sophisticated lightweight and energy-absorbing porous structures, including lattices, honeycomb, and triply periodic minimal surface (TPMS) structures [1]. Selective Laser Melting (SLM) as the most common additive manufacturing (AM) technology has made it possible to fabricate complex structures with exact dimensions. The structural properties of porous materials such as pore size distribution, pore shape, and specific surface areas play a vital role in the quality and mechanical behavior of these structures. They can be optimized to obtain the required properties [2]. Thus, this study involves the evaluation of porous structures fabricated using SLM as well as investigation of the influence of unit cell geometry.

1.2. Objectives

The objective of this thesis is to develop models that can demonstrate the mechanical properties of architectured IN718 materials processed on an EOS M290 metal 3d printer. The other aim is to observe the deformation mechanisms governing the mechanical behavior of 3D printed metallic structures. The result of this project enables the development of lightweight structures that will potentially open new research areas on manufacturing various consumer products with 3D architectures.

1.3. Approach

In the present study, first, the investigation of structural properties of porous materials such as porosity type, porosity level, and pore size were carried out. Then, the influence of each parameter on hardness, mechanical response, microstructure, and composition has been studied. Several experiments were performed on porous SLM Inconel 718 (IN718) superalloys: i) Failure tests: to examine, ductility yield strength and critical stresses of samples; ii) Microstructure analysis: to investigate microstructure properties of the porous Inconel 718 super alloys before and after failure; iii) Finite element analysis: to predict the behavior of porous parts under loading conditions; and iv) Compositional, roughness, and hardness testing: to reveal the effect of the structural properties on the performance of the porous parts.

Finally, it was shown that functional Inconel 718 parts with variable porosity and desirable mechanical properties could be fabricated.

1.4. Outline

Chapter 1 is about the motivation, objectives, and contribution of this research work. Chapter 2 details state of the art in SLM of Inconel 718, lattice structures, and optimization techniques. Chapter 3 explains the lattice design, material preparation, manufacturing process, and experimentations conducted in this study. Chapter 4 interprets the results and observations in microstructure, mechanical behavior, finite element analysis, composition, hardness, and roughness. Chapter 5 illustrates the significant contributions of this work and propose other possible areas where the results of this research can be used.

1.5. Contribution

The contribution of this research will be an understanding of the needed structural properties of architectured materials for high-end applications where high strength, lightweight, and shock-absorbing properties are required. Moreover, the influence of the structural properties of porous materials on the microstructure and mechanical behavior will be revealed.

Chapter 2. Background and Literature Review

2.1. History and Applications of Inconel 718 Superalloy

Generally, a metallic material that deals mostly with high temperatures and heavy loading conditions without any deterioration in its mechanical and chemical properties is termed as a “Superalloy” [3]. In 1906, Monel was the first one who developed a corrosion-resistant nickel superalloy. Later, in the 1940s, Wiggin Alloys in Hereford, England, developed Inconel superalloys to be used in jet engines. In 1959, the International Nickel company developed Inconel 718 superalloy after several attempts to build a robust solution- strengthened, non-age hardenable alloy [4]. Inconel 718 superalloy has a high level of nickel content (50-55%) that enables its applications in harsh conditions such as elevated temperatures, oxidation, and corrosion [5-9]. Oxidation resistance, high-temperature performances, good creep and fatigue properties, and high hardness are amongst the positive features of this superalloy [10]. The combination of these properties enabled the utilization of Inconel 718 superalloy in military engines in the early 1960s. In the later stages of the decade, this alloy was also used in applications such as gas turbines because of its high performance, price, and presence of low cobalt and high iron content [4, 11]. Later, per API standards, Inconel 718 supper alloy received significant attention as a material for nuclear, oil, and gas industries, such as drilling tools, downhole equipment, and surface wellheads [12-15].

2.2. Chemical Composition

The Unified Numbering System (UNS) identifier of Inconel 718 is known to be N07718. It is a precipitation-hardening nickel-chromium alloy containing significant amounts of iron, columbium, and molybdenum, along with lesser amounts of aluminum and titanium. Table 1 reports the chemistry of this alloy.

Table 1. Composition of Inconel 718 [4, 11].

Element	Composition (%)
Carbon	0.08 max
Manganese	0.35 max
Silicon	0.35 max
Sulfur	0.015 max
Phosphorous	0.015 max
Chromium	17.00 to 21.00
Cobalt[A]	1.0 max
Molybdenum	2.80 to 3.30
Columbium + tantalum	4.75 to 5.50
Titanium	0.65 to 1.15
Aluminum	0.20 to 0.80
Iron[B]	Remainder
Copper	0.30 max
Nickel	50.00 to 55.00
Boron	0.006 max

[A] If determined
[B] Iron shall be determined arithmetically by difference

The microstructure and mechanical properties of Inconel 718 highly depends on the contents of δ, γ′, and γ″ phases in Inconel 718 [16]. It can be found that there are small inclusions of NbC, TiC, and Ti (CN) [16]. Apart from the presence of primary intermetallic compounds of δ, γ′, and γ″ phases. It is explained as (i) γ′ having a composition Ni_3(Al, Ti) and a cubic (L12) crystal structure, (ii) γ″ having a composition Ni_3Nb and bct (D022) crystal structure, and (iii) δ having a composition of Ni_3Nb and an orthorhombic (D0a) crystal structure. The existence of local Nb content and residual δ particles might influence the precipitation kinetics. The δ-phase can contribute to grain growth control, but in its absence, other precipitate particles, like carbides, could also provide grain growth inhibition [17].

2.3. Fabrication of Inconel 718

2.3.1. Conventional Manufacturing of Inconel 718

In the past, Inconel 718 superalloy has been developed and applied in the cast, wrought, and powder metallurgy forms (Figure 1) [4]. Casting is the oldest manufacturing process in which molten liquid is poured into a mold with a hollow cavity of the desired shape. After solidification, the part is ejected out of the mold. Inconel 718 can be used in the process of die casting, but additional refinement and optimization are mandatory. The die-cast Inconel 718 is known for its smooth fatigue properties [18]. Wrought refers to "worked". In this procedure, the hot metal is removed from the furnace and formed with a hammer until the final form is achieved. This method was widely used in the 19th century. The process is a result of plastic deformation in which the shape of the material is changed permanently. These days, this process is mainly used for decorative applications. Even though the wrought process of Inconel 718 was a huge success, there was still scope for improvement in temperature capability and its time-dependent fracture behavior [4]. Powder metallurgy (PM) has been widely used to fabricate Inconel 718. They are applied in turbine engines since the 1970s because of their superior mechanical properties and high-temperature capability [19, 20]. The processing routes of PM superalloys are direct powder hot compaction (mostly by Hot Isostatic Pressing) and hot working processes[3, 20]. The hot worked alloy possesses uniform microstructure and better mechanical properties, but the process is known to be expensive. Compared to wrought Inconel 718, the mechanical properties of the PM processed alloy using the new HIPing procedure are excellent [21].

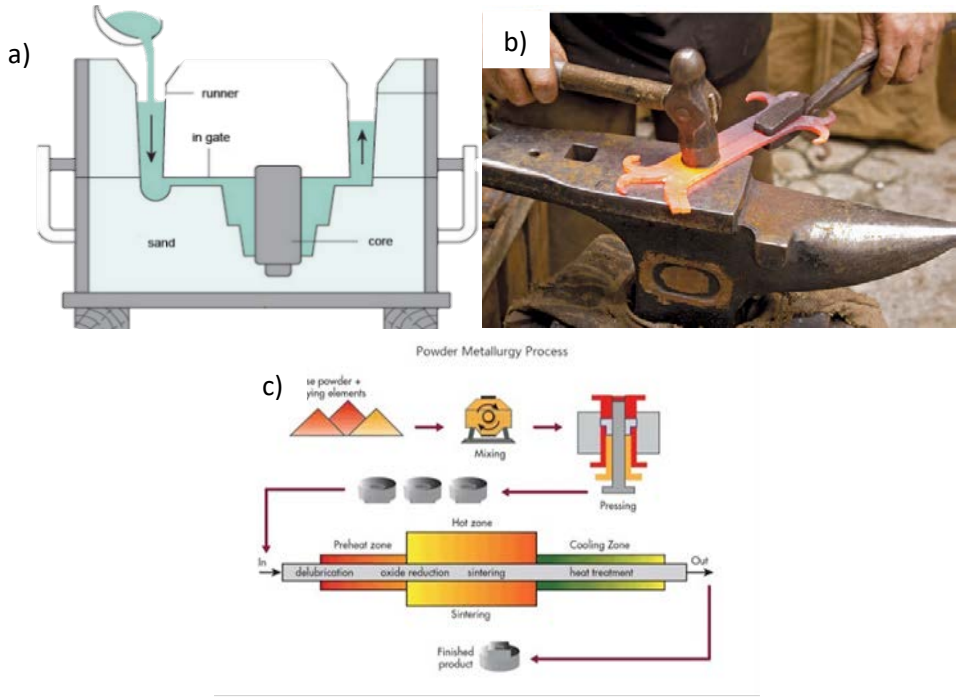

Figure 1. The schematic of a) casting, b) wrought, and c) powder metallurgy procedure.

2.3.2. Additive Manufacturing of Inconel 718

In recent years, laser-based additive manufacturing (LBAM) technologies have been widely used to fabricate Inconel 718 alloys. LBAM can build complex Inconel 718 structures that possess high strength without strain age cracking and can overcome the difficulties of conventional manufacturing. The LBAM can be classified as Powder-bed fusion (PBF), or Powder-bed based technique. Flow-based or Direct Energy Deposition, and Sheet Lamination. Powder-bed based is the most used technique among LBAM because the parts fabricated using this process have better geometrical accuracy typically. Powder-bed based is a fast process for functional, durable, and consumer parts. This process allows the fabrication of high overhanging angles (0 to 45 degrees from horizontal plane), complex geometries, components with high strength, stiffness, and chemical-resistance properties. Batch production of multiple parts, called nesting, is also possible with powder-bed based processes. This process is a good substitute for the injection molding technique as these parts have reliable mechanical properties. Below, the different types of powder-bed based manufacturing are described:

Selective Laser Melting (SLM): SLM involves slicing the CAD file into several layers with a certain thickness. Each layer is fabricated with the employment of appropriate combinations between the processing parameters (*e.g.*, Laser power, Hatch space, layer thickness, and scan speed) [22-27]. Based on the specified thickness, a roller or blade deposits a powder layer. The thickness range is typically ranging from 20 to 100 μm [28-33]. This step is followed by the melting of powder with laser power depending on the geometrical information of the sliced CAD file. The building piston moves down, and similarly, the next layer is deposited after solidification. The final 3D part is obtained by the repetition of this process (See Figure 2). After the procedure is completed, the supports and loose powders are removed [34-45]. The chamber should be filled with argon gas to prevent oxidation. The properties of the final highly depend on the process parameters. These parameters, such as laser power and scanning speed, should be selected wisely as it dramatically affects the part's properties such as porosity, hardness, and mechanical properties [34, 46-53].

SLM helps to create fully functional parts from metals without using any intermediate binders or additional post-processing steps after the primary process is completed. This process results in a homogeneous distribution of alloying elements without the formation of oxides that has a significant impact on the mechanical properties. The economic and efficient use of material with recycling is possible with this process that helps the ability to use 100% percent material, which is the most significant advantage of this method. SLM allows producing more efficient components as it provides unlimited geometrical design freedom without any limitations. There are no toxic chemicals utilized in this process [54].

The cost of manufacturing is one of the disadvantages due to the expensive metal powders. There is always a need for proper particle size and morphology. The long build times are associated with the processing of these small material quantities per unit time. Periodic cellular lattice structures can save expensive material quantity by reducing build time and energy consumption in the SLM process [55]. High cooling rates are typical in SLM that results in high internal stresses and dislocation densities. The cooling

rates around 106 K/s are observed during the process [56]. Recycling affects the powder material properties that, in turn, affect the mechanical behavior of the fabricated parts [55, 56].

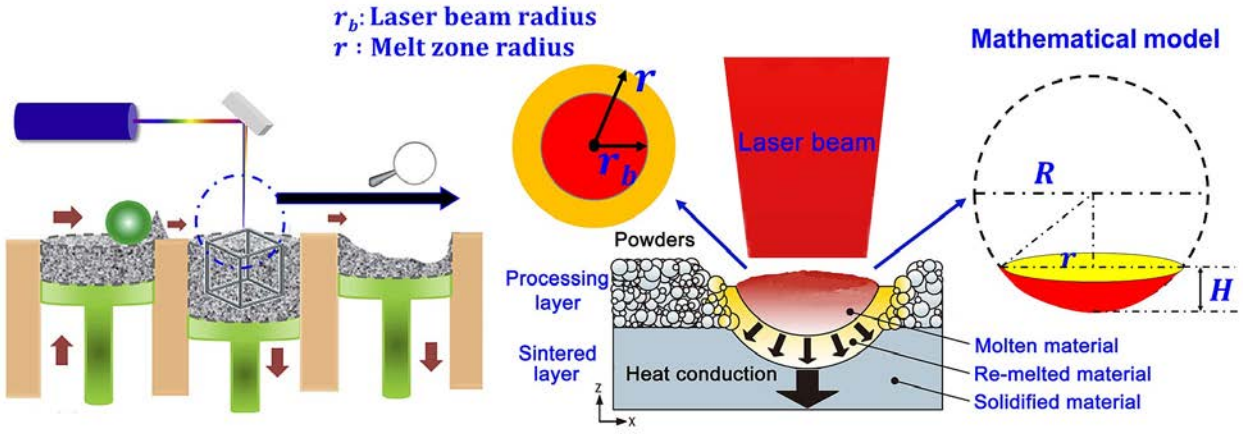

Figure 2. Schematic representation of the Selective Laser Melting (SLM) method [57].

Selective Laser Sintering (SLS): This technique is a PBF process that partially sinters the powder material with a high laser power source. The significant difference between SLS and SLM is the level of powder melting, which results in different material properties of the fabricated parts. Here, the laser is aimed at points automatically in space defined by a 3D model. This binds the material together, and the material is formed. SLS has been mainly used for rapid prototyping. It has been used for low volume production of components and expanding for consumer-based products. The main disadvantage is the presence of porous surfaces and the need for additional post-processing methods like cyanoacrylate coatings or Hot isostatic pressing. The disadvantage of this method is the weak mechanical property exhibited by the fabricated part. This also makes the part less dense [58].

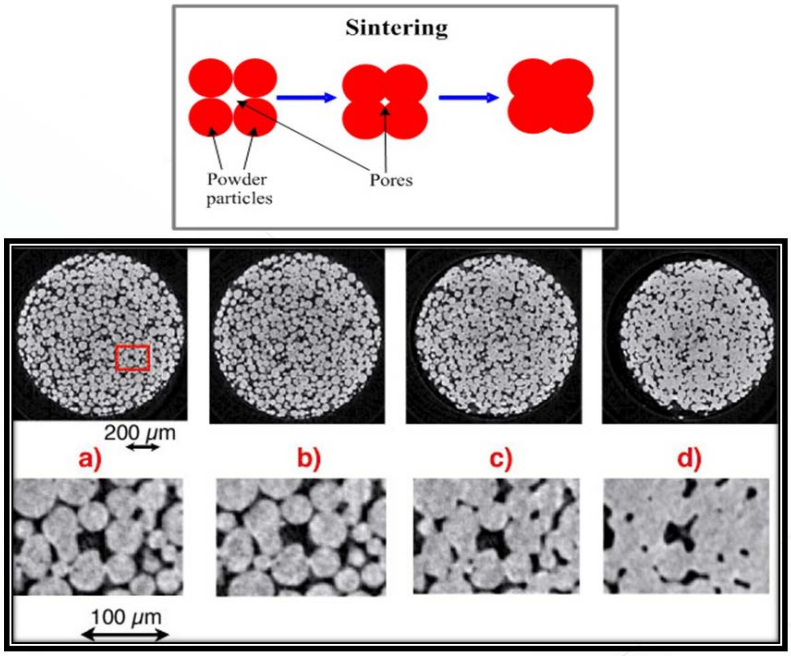

Figure 3. Selective Laser Sintering (SLS) Process method [59].

Direct Metal Laser Sintering: The DMLS process is one of the effective PBF techniques that involve a single powder with two different grain sizes or two different grain types. This process begins with the full sintering of each metal powder layer, starting from support structures next to the base plate followed by the part. A recoater blade moves across the platform to deposit the next layer. This is followed every time after a cross-sectional layer is built until the entire process is completed. The DMLS fabricated metal parts are mostly without internal defects. This process provides the ability to get rid of balling phenomena. The reason behind this is that the particle inside the metal is fused completely [60, 61].

Up to now, several groups have implemented AM to produce and evaluate Inconel 718 parts. Table 2 shows a list of current publications on AM technologies that have been used for processing Inconel 718. The type of the machines, the laser power, the powder composition, as well as the substrate composition, are summarized in Table 2.

Table 2. A list of current publications on SLM technologies that have been used for processing IN718.

AM Technology	Machine Type	Laser Power (W)	Scanning Velocity (mm/s)	Hatch Space (µm)	Layer Thickness (µm)	Powder size (µm)	Author
SLM	-	110, 110, 120, 130	600, 400, 400, 400	-	-	15- 45	Jia *et al.* [62]
EBM	Arcam® EBM S12 machine	-	-	-	50	-	Raghavan *et al.*. [63]
SLM	SLM 250HL machine	100 W	540	120	30	30	W.Tillmann *et al.* [64]
EBM	ARCAM A2 SEBM System	594 W	2200 to 8800	100, 37.5	-	-	Korner *et al.* [65]
EBM	EBM 12 SYSTEM FROM ARCAM AB	-	918	-	70	47 ± 23	Hinojos *et al.*[66]
SLM	Concept M2 machine	180-220	-	-	30 to 45	-	Lambert, Dennis M [67
DLD	IPG Photonics 5 kW system equipped with an ABB robot	5000	-	-	-	-	Y.N.Zhang *et al.* [68]
SLM	SLM 280HL	250, 950	700, 320	120, 500	50,100	20 to 60	V.A.Popovich et al. [69]
LAM	-	550	-	-	-	-	Yuan Tian *et al.* [70]
SLM	DMP PROX300	450	1000 to 1800	50 to 90	70	5 to 25	K.Moussaoui et al. [71]
SLM	EOS M270	200	800 to 1200	-	-	17 µm	Amato, K. N., *al.* [72]

2.3.3. Additive Manufacturing of Porous Inconel 718

The limitations of conventional manufacturing techniques made the realization of porous topologies complex even though they were discovered more than a century ago. But now, due to the advancements in manufacturing methods, the task became possible over a wide range of length scales [73].

The methods of fabricating periodic porous structures involve liquid state, solid-state, and vapor deposition methods. In these methods, the shape and size of the pores can be randomly adjusted by changing the parameters of the processes, but only stochastic structures are possible.

LBAM is capable of manufacturing porous metals with definite shape and architecture [55]. SLM is known for its accuracy and resolution among LBAM techniques; hence, they are a better option to print porous structures. The manufacturability of porous parts, however, highly depends on the porosity type.

The nature of the gyroid unit cell can be described as circular and smooth struts along with a spherical core. The inclination angle of circular and flat struts varies with the core, and the layers grow gradually with changes in area and position. This helps one layer supporting the adjacent during the SLM process, making the gyroid structures are self-supporting. This also makes the SLM process comfortable, versatile, and opens the way for constructing advanced lattice unit cells on a large scale without the need for support structures.

Compared to SLM, other LBAM methods show significant variances in mechanical properties and microstructure of parts. It is possible to even improve the dimensional and mechanical properties of SLM parts by choosing optimum process parameters. The most significant process parameters are laser power, scan speed, hatch spacing, and layer thickness. Dimensional accuracy, microstructure, and mechanical behavior can be controlled by energy density. The energy density can be calculated from Equation 1:

$$E = \frac{P}{h.v.t} \qquad \text{Equation 1}$$

Where,

E – Energy Density; P- Laser Power; v- Scan Speed; t- Layer Thickness; and h- Hatch spacing.

2.4. Cellular Structures

Light-weight metal cellular structures are unique as they can offer high strength, low mass, and energy absorption characteristics along with excellent thermal and acoustic insulation properties [74]. The classification of cellular structures is stochastic porous structures and periodic cellular structures. The

stochastic structures, in general, are randomly organized with open or closed voids. But, the periodic structures are typical in nature structured with repeating unit cells. Examples of cellular structures are foam, honeycomb, sponges, folded materials, and lattice structures.

The periodic structures show superior mechanical properties with adequate strength and stiffness. In periodic cellular structures, the structural features can be easily controlled in a way to demonstrate better load carrying capacities and higher surface area when compared with the stochastic structures [75]. This feature makes periodic cellular patterns to be applied to metals yielding advanced multifunctional performance in products that are used in aerospace, automobile, and medical applications [76, 77].

2.4.1. Periodic Cellular Structures - Lattice

The lattice structure falls under the category of cellular materials and is commonly used interchangeably in the literature. Lattice structures are mainly characterized by open pores and built with an organized structural orientation of unit cells. The arrangement of unit cells in a specific order can also be stated as reticulated. The term ‘reticulated’ can be used for lattice arrangement. The deformation behavior can be found in the form of stretching or bending, thereby stating the failure of any unit cell-based geometry. Unlike stochastic meshes, the reticulated meshes were found to have better mechanical properties when compared with each other. Thus, the unit cells proved satisfactory properties than the random stochastic structures [78]. Mechanical properties are tailored by unit cell geometry and topology. In these lattice structures, the unit cells are classified based on their formation or deformation behavior [79].

The examples of lattice structures are BCC, BCC-Z, FCC, FCC-Z, honeycomb, and sandwich panels structures [80]. Lattice terminology is based on conventions in crystallography with additional designation for vertical (Z) struts[81]. The BCC, BCC-Z, FCC, FCC-Z lattice structures comprising strut-like members can be classified as stretching-dominated and bending-dominated structures [82]. Stretching-dominated structures are known for stiffness and strength, while bending-dominated structures have a better specific energy absorption behavior for a high-stress plateau under compression. The body-centered cubic

(BCC) is a typical type of bending-dominated structure, and this structure has received considerable attention and been experimentally and theoretically analyzed for its individual mechanical and energy-absorbing performances [83-86]. The BCC-Z and FCC-Z can be explained to be probably as under-stiff but high compressive strength and stiffness along z-direction struts, according to Leary *et al*. [87]. The honeycombs are also known as prismatic structures. They can handle definite flows or loads. However, these structures fail due to thin walls that reduce lateral strength and stiffness. Sandwich panels are considered to be an improvement of honeycombs that are made of two material sheets covering the cellular structure. This design is explained to handle compression and tension while the honeycomb cells carry the shear load.

2.4.2. Periodic Cellular Structures- Triply Periodic Minimal Surface (TPMS)

The triply periodic minimal surface (TPMS) geometry is one of the types that fall under R3 that is known as the rank-3 lattice of translations. These geometries are symmetrical and crystallographic. The examples of the symmetries are cubic, tetragonal, rhombohedral, and orthorhombic. The other types are Monoclinic and triclinic but are hard to parametrize [88]. These structures are derived from natural structures that can be observed in cell membranes [89], block copolymers [90], and equipotential surfaces in crystals [91]. Schwarz was one of the first examples of TPMS described by Hermann Schwarz in 1865 [92]. Alan Schoen described 12 new TPMS based on skeleton graphs spanning crystallographic cells [93]. Even though Schoen's structures were famous in science, there was no mathematical proof for it until H. Karcher proved their existence in 1989 [94]. Using conjugate surfaces, many other surfaces were found. Weierstrass represented more straightforward examples, but Discrete differential geometry was used for the representation of these methods [95].

2.5. Mechanical Properties

Various aspects that affect the mechanical properties of porous structures are discussed in this section. The mechanical properties of lattice structures, particularly, compressive strength and young's modulus highly depend on cell topology and porosity level [80, 87]. Mechanical properties are also affected

by the loading response of struts present in the lattice, which are either stretch-dominated or bending-dominated [80]. One should also consider process parameters and build orientation as they also deviate the properties without the consideration of optimum values.

Leary *et al.*[87] evaluated the performance of lattice AlSi12Mg parts such as FCC, FCC-Z, BCC, BCCZ, and FBCCZ under quasi-static uniaxial compression. All the specimens showed a large ratio of collapse stress to the plateau stress. They also concluded that the FBCCZ structure demonstrated stable crushing behavior and excellent energy absorption characteristics after plotting energy absorption up to a strain integration limit of 10%. S.J.Al-Saedi *et al.* [96] studied F_2BCC SLM Aluminum lattices and observed various collapse regions followed up with long plateau before the structure was fully crushed. The elastic stage was relatively linearly proportional. In another study, Mazur *et al*. [97] conducted tests on Ti6Al4V lattice specimens. They showcased that the specimens had comparatively high initial strength that led to softening after the initial collapse.

Sing *et al.* [98] performed compression test on cellular Ti4al6v structures fabricated with different SLM processing parameters. It was shown that the elastic constant of the lattice structures varies between 1.36 ± 0.11 GPa and 6.82 ± 0.15 GPa. They also proved that the mechanical properties were affected by laser power, scanning speed, and layer thickness.

Wauthle *et al.* [99] studied the static behavior of five titanium lattice structures processed with different build direction. The diagonally oriented sample was inferior to that of horizontally and vertically oriented samples. The latter two structures had near-identical properties. It was concluded that the compressive strength and the stiffness of the diagonally oriented sample were, on average, 35% lower to the vertically oriented sample, irrespective of heat treatment condition.

Maskery *et al*. [100] performed uniaxial compression tests on Al-Si10-Mg BCC lattice structures using an Instron 5969 universal testing machine. They observed a significant structural collapse at around 9% strain, where almost 95% of the structure's strength was lost. This was also followed by an initial period

of linear elasticity and non-linear behavior, after which cell struts began to bend due to the applied compressive load. A little bending occurred resulting in the struts experiencing brittle fracture [101] and hence a diagonal (45°) shear bend [102, 103]. It was understood that the structure was subsequently weakened and failed to recover its pre-collapse strength even as the strain increases up to 50%.

Xiao *et al.* [104] studied the performance of three types of lattice structures, namely FCC, VC, and ECC structural lattice, fabricated with 316L Stainless steel. They observed that the structures experienced plastic collapse following with a long yield plateau. At some points, the trusses combined and formed a densified area that led to a sharp rise in the stress-strain curve. With higher porosity level, they also observed a weaker lattice structure, less yield strength, plateau stress, inferior mechanical properties, and a lower energy absorption capability.

2.6. Microstructure Analysis

SLM processed lattice parts are prone to some avoidable deficiencies that can be identified through microstructure analysis. SLM-fabricated components are often exposed to geometric defects, due to various factors such as suboptimal processing parameters [105], or even internal defects due to incomplete filling by the laser beam. Residual stresses that are caused by thermal gradients also affect the components also leads to geometric defects and deformation. The staircase effect, a general geometric error of AM processes, occurs in SLM too. These defects not only affect manufacturability, dimensional accuracy, and surface roughness of SLM lattice structures but also associated with mechanical and biological properties of fabricated components. Microstructure analysis helps us to observe the manufacturing quality of struts after fabrication and let us confirm the optimum build parameters. The rapid solidification in SLM, which is also directional, affects local microstructure. For instance, directional solidification results in a preferred crystallographic orientation that can impact the mechanical properties [99, 106].

Choy *et al.* [107] studied the struts of four different SLM-fabricated Ti6 lattice structures, which consisted of two different orientations with cubic and honeycomb cellular units, respectively. In all specimens, it was found that the morphologies of the top and side surfaces of the lattice struts were different.

At the top surface, clear and continuous melting could be observed with powder adhesion at the edge of along with side surfaces of the lattice struts. Powder adhesion at the bottom side of the horizontal struts was higher than the diagonal struts. Finally, it was observed that the adhesion of powder greatly affected the dimensional accuracy of the fabricated lattice structure. They also suggested that the differences between the designed and measured strut diameters were comparatively less for larger struts, indicating that the dimensional accuracies are lower if the strut size is smaller due to relatively higher degree of powder adhesion. Yan *et al.* [55] reported the presence of bonded particles on the surfaces of struts, and related them to the balling phenomenon or partial melting phenomenon of raw stainless-steel particles on the boundary of solid struts. In SLM, a completely melted material gives rise to beads being formed mainly on laser melted surfaces perpendicular to the building direction [108].

Santorinaios *et al.* [109], McKown *et al.* [110] and Pattanayak *et al.* [111] observed narrow and short cracks having a width of below one μm and a length of fewer than 20 μm within the struts of SLM-fabricated lattices [55]. Generally, cracks can be attributed to the existence of high residual stresses during the process of SLM. In another work, Gangireddy *et al.* [112] studied the high strain rate mechanical behavior of Octet Ti6 lattice structure. The lattices showed fully densified interior areas composed of a homogeneous microstructure of acicular martensitic needles without any pores/defects. This observation was the typical result of the rapid cooling rates during SLM process [113, 114].

The microstructures of SLM-produced Stainless steel lattice specimens with F_2BCC porosity type were described by Patrick Köhnen *et al.* [115]. The majority of the grains were columnar grains elongated with a high aspect ratio featuring a length of >200 μm. Grain growth was not restricted by the height of the melting tracks due to epitaxial growth.

To study the influence of process parameters, Qui *et al.* [103] fabricated AlSi10Mg diamond-type lattices using two different laser powers, 150 W and 400 W, generated the SEM micrographs, and measured the strut diameters. The images clearly showed that higher laser powers resulted in thicker struts with a linear relationship. The struts with increased laser power also demonstrated more geometrical when

compared with that processed with low laser power. This observation can be used for optimizing parameters when precise dimensions and shapes are required for a particular application. In addition, with an increase in the laser power, an increasing number of partially melted powder particles were found to adhere to the strut surfaces [116-118].

Chapter 3. Materials and Methods

3.1. CAD Design

To study the influence of porosity type, as seen in Figure 4, four different lattice structures including BCC, BCC-Z, FCC, FCC-Z and three different triply periodic minimal surfaces (TPMS) structures including Schwartz, Gyroid, and Diamond models were designed with the same level of porosity (45%). Further, to investigate the effect of porosity level, three BCC lattice structures with porosity levels of 30%, 45%, and 60% were designed. All designed porous parts were made of 64 unit cells (4 by 4 by 4), each having the dimensions of 2 mm x 2 mm x 2 mm. Also, two plates with a thickness of 1.5 mm each were considered at the top and bottom to support compression testing. Details about the design procedure of these abovementioned porous structures are provided below:

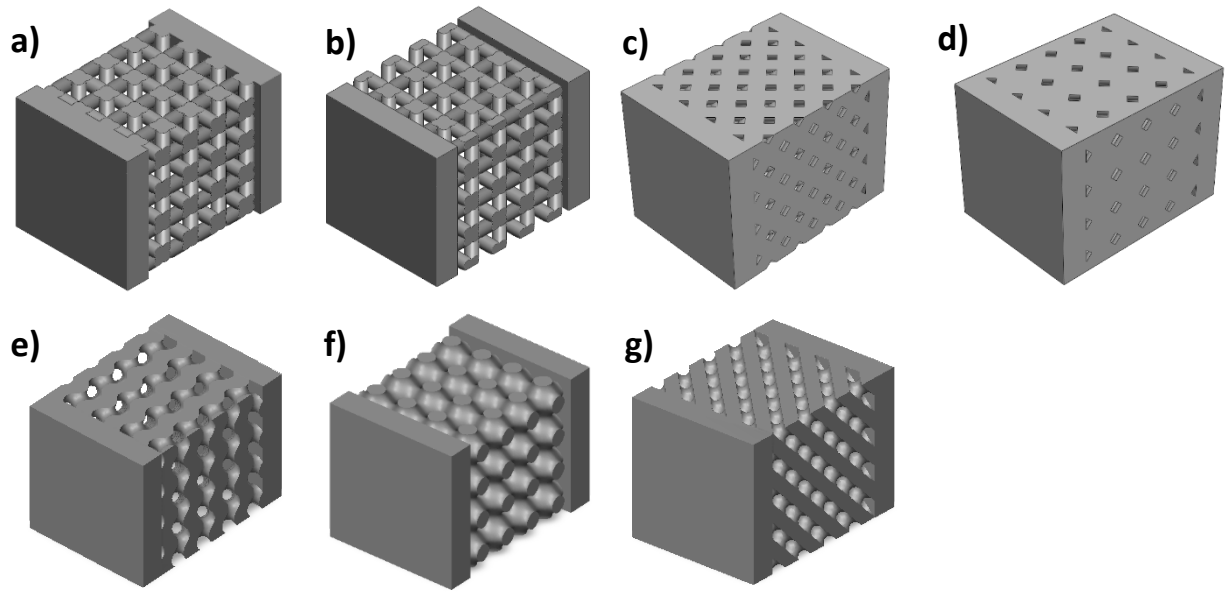

Figure 4. Designed porous structures with same level of porosity (45%) and different porosity types: a) BCC; b) BCC-Z; c) FCC; d) FCC-Z; e) Gyroid; f) Schwartz; g) Diamond.

3.1.1. Periodic Cellular Structures- Lattice Structures

The BCC, BCC-Z, FCC, FCC-Z lattice structures were modeled using Solidworks (version 2018-2019, Dassault Systems, USA). Figure 5 represents the unit cells of the lattice structures, each having a dimension of 2 mm x 2 mm x 2 mm. The CAD file creation process started with the creation of cylinders

that are considered as struts with precise dimensions across X, Y, and Z axes. Extruded cylinders were followed into linear pattern combined and cut to form a lattice cube of 8 mm x 8 mm x 8 mm. Two plates, each with a thickness of 1.5 mm, were added at the top and bottom to support compression testing.

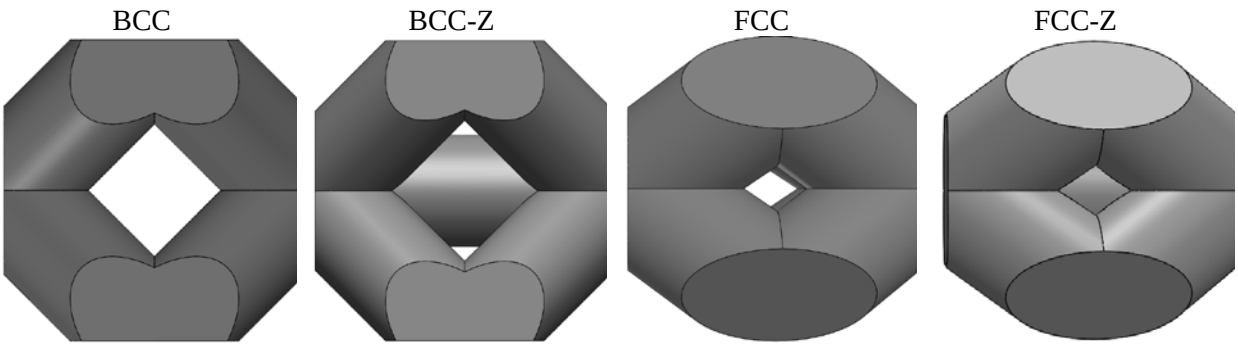

Figure 5. The designed unit cell for different types of lattice structures: BCC, BCC-Z, FCC, FCC-Z.

The dimensions governing the porosity were based on the diameter of the cylinders. The relation between the diameter and porosity level (PL) for each lattice structure was derived and are presented in equation 1-4 and Figure 6.

$$PL_{BCC} = 61.686D^3 - 136.67D^2 + 0.2572D + 99.9 \quad \textit{Equation 1}$$

$$PL_{BCCZ} = 78.455D^3 - 160.1D^2 + 4.101D + 99.2 \quad \textit{Equation 2}$$

$$PL_{FCC} = 48.737D^3 - 110.86D^2 - 0.0957D + 100.01 \quad \textit{Equation 3}$$

$$PL_{FCCZ} = 42.758D^3 - 86.889D^2 - 23.179D + 103.69 \quad \textit{Equation 4}$$

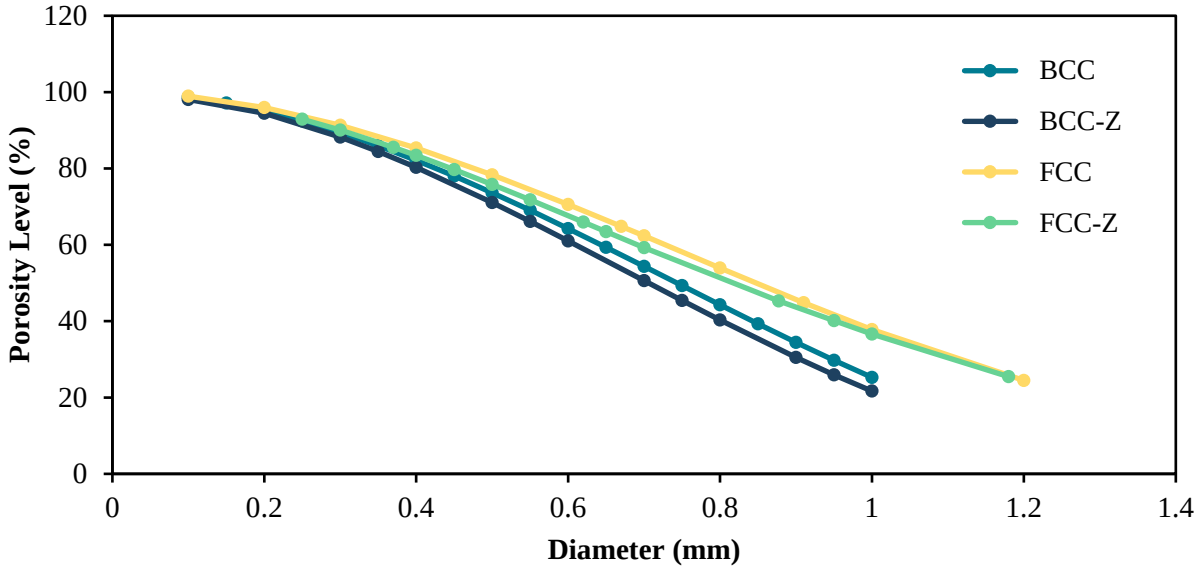

Figure 6. The relation between the struct diameter and porosity level for BCC, BCC-Z, FCC, and FCC-Z lattice structure.

3.1.2. Periodic Cellular Structures-TPMS

A study by Von Schnering and Nesper [119] helped to obtain the nodal approximations of Schwartz, Gyroid, and Diamond from a series of mathematic equations, as represented in equations 5-7, respectively. Constant K in the equation effectively controls the porosity level of the TPMS structures.

Schwartz $F(x,y,z) = \cos(2\pi x) + \cos(2\pi y) + \cos(2\pi z) - K$ *Equation 5*

Gyroid $F(x,y,z) = \sin(2\pi x).\sin(2\pi y).\sin(2\pi z) + \sin(2\pi x).\cos(2\pi y).\cos(2\pi z) \cos(2\pi x).\sin(2\pi y).\cos(2\pi z) + \cos(2\pi x).\cos(2\pi y).\sin(2\pi z) - K$ *Equation 6*

Diamond $F(x,y,z) = \cos(2\pi x).\sin(2\pi y) + \cos(2\pi y).\sin(2\pi z) + \cos(2\pi z).\sin(2\pi x) - K$ *Equation 7*

The coordinates of the surfaces of the porous parts were created using Mathmod v10 software (Figure 7 a-c). Then, Materialise Magics (Materialise 2020, Leuven, Belgium) was used to create the surfaces. For each structure, the software was utilized to convert a shell CAD file (STL) to a solid structure (IGES) (Figure 7 d-f).

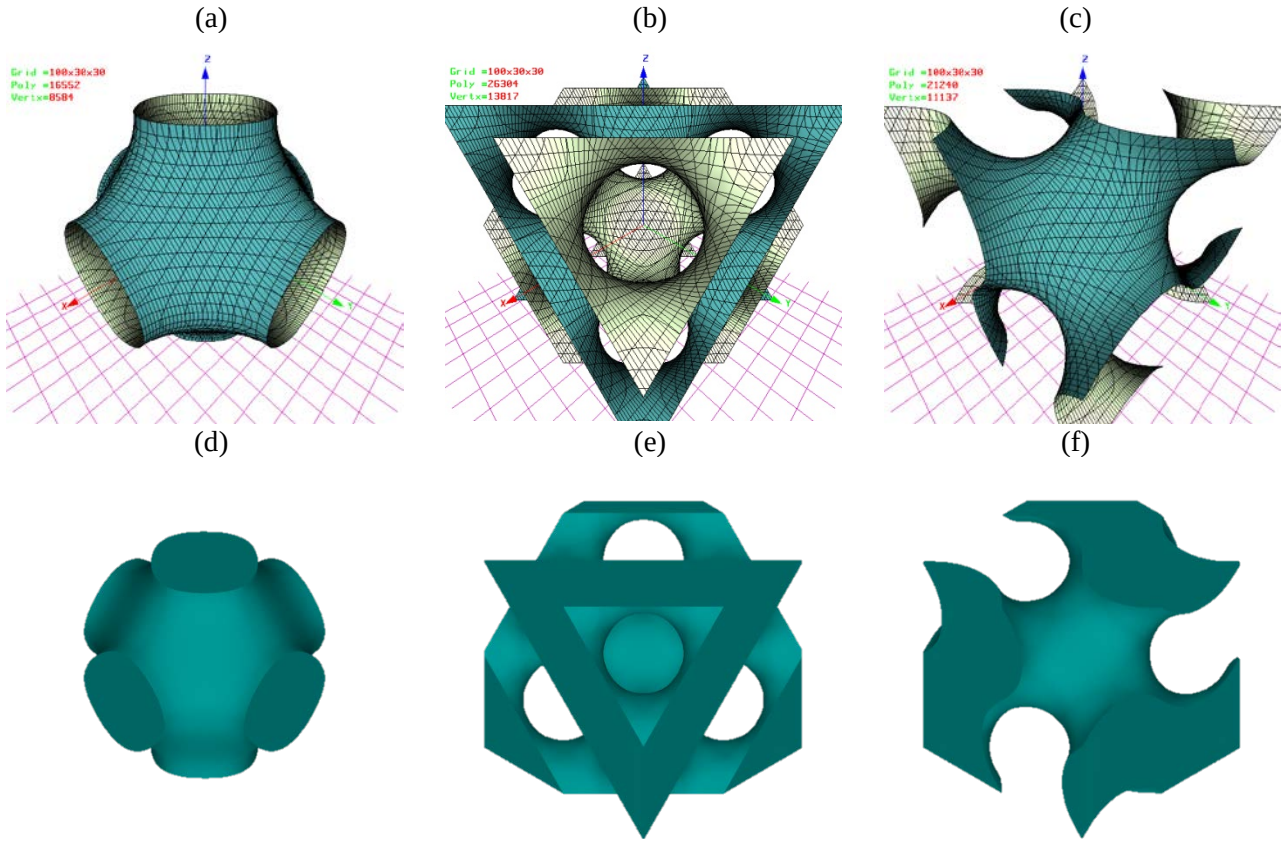

Figure 7. The surfaces and solid structures are generated for (a), (d) Schwartz-type; (b), (e) Diamond-type; and (c), (f) Gyroid-type.

For Schwartz, Diamond, and Gyroid, the porosity level can be reasonably approximated in the range of 10 % to 90 % with the linear equations described below.

$PL_{Schwartz} = 28.742K+49.99$ Equation 3.8

$PL_{Gyroid} = 42.284K + 50.12$ Equation 3.9

$PL_{Diamond} = 32.783K + 50.12$ Equation 3.10

Open porous cubic TPMS CAD files with 8 mm x 8 mm x 8 mm dimensions were designed with a constant porosity level of 45%. Two plates, each with a thickness of 1.5 mm, were added at the top and bottom to support compression testing. A total of 3 samples of each TPMS type were generated.

3.2. Part Preparation for Additive Manufacturing

The lattice structures and TPMS CAD files were imported into Magics software (Materialise 2020, Leuven, Belgium) as STL format. A 3 mm height block support structure (thickness =

0.3 mm; gap = 1 mm) was considered for each sample. All samples and associated supports were imported to EOSPRINT 2 (EOS GmbH, Electro-Optical Systems, Krailling, Germany). Then, a recommended set of laser processing parameters was assigned to each sample, i.e., laser power (*P*) of 285 Watt, scanning speed (v) of 960 mm/s, hatch spacing (*h*) of 110 µm, layer thickness of 40 µm, and a stripe scan strategy. The exposed laser angle between each layer was every 67 °. The energy density of 67 J/mm^3 was calculated from Equation 8.

$$E = \frac{P}{h.v.t} \qquad \textit{Equation 8}$$

3.3. Powder Preparation and Fabrication

IN718 powder was obtained from EOS Engineering Inc. (Austin, TX). The powder was sieved with a mesh size of 90 µm to avoid inhomogeneity in the distribution of the particle size. Table 3 represents the chemical composition of the employed Inconel 718 powder. The prepared files were transferred to a DMLS EOS M290 metal 3D printer (EOS GmbH Electro Optical Systems, Germany), equipped with a 400 W Ytterbium fiber laser (See Figure 8). All samples were fabricated in 200 sliced layers.

Table 3. Chemical composition of commercial EOS Inconel 718 powder [120].

Compositional Element	**Percentage (%)**
Ni	50-55 wt%
Cr	17-21 wt%
Nb	4.75-5.5 wt%
Mo	2.8-3.3 wt%
Ti	0.65-1.15 wt %
Al	0.20-0.80 wt%
Co	≤ 1.0 wt-%
C	≤ 0.08 wt-%
Si, Mn	Each ≤ 0.35 wt-%
P, S	Each ≤ 0.015 wt-%
B	≤ 0.006 wt-%
Fe	Balance

Figure 8. EOS M290 metal 3d printer equipped with a 400-Watt Laser.

After the fabrication was done, the parts were removed carefully with safety precautions. The remaining powder, if it exists on the parts were brushed off, and the supports were removed using a bandsaw.

3.4. Mechanical Testing

Compression tests were conducted with the help of a 100 kN MTS Landmark servo-hydraulic test platform (MTS Systems Corporation, Eden Praire, Minnesota, USA), which is shown in Figure 9. A strain rate of 10^{-4} sec^{-1} was applied during loading. All samples were tested until failure, and the load-displacement graphs were plotted. Using Digital Image Correlation (DIC) tools, the deformation profile of the parts under loading was also captured.

Figure 9. 100 KN MTS Landmark servo-hydraulic test platform.

3.5. Sample Preparation for Microstructure Analysis

An Allied E-PREP 4™ Grinder/Polish machine (Allied High-Tech Products, Inc., Compton, CA) was used for grinding and polishing (See Figure 10). The abrasive discs used for grinding was made of Silicon Carbide (SiC) (320-1200 Grit Size). To check if the scratch pattern was uniform, the surface was inspected through metallographic microscope XJP-H100 (Amscope, Irvine, CA). If there happened to be any deformation due to grinding, one μm diamond suspension on DiaMat polishing cloth with GreenLube lubricant was performed. Polishing was completed with the help of 0.04 μm colloidal silica suspension on a Chem-pol polishing cloth. After the procedure was completed, the platen was wiped with water and spin-dried to remove any existing debris. Finally, The sample and fixture were cleaned with micro-organic soap, rinsed with isopropyl alcohol, and then dried using compressed air spray [121].

Figure 10. Allied E-PREP 4™ Grinder/Polish.

3.6. Scanning Electron Microscopy (SEM)

SEM tests were conducted with the help of a Hitachi S-3000N variable pressure SEM microscopy (Hitachi, Tokyo, Japan) in Characterization Center for Materials and Biology at the University of Texas at Arlington (CCMB-UTA). The machine worked at 20 kV in the backscatter electron emission or secondary electron imaging nodes. (Figure 11)

Figure 11. Hitachi S-3000N Scanning Electron Microscope.

3.7. X-ray diffraction (XRD)

X-ray diffraction (XRD) machine was used to determine the crystal and compositional structures of the samples. The equipment used for XRD analysis was the Bruker D8 Advance X-ray diffractometer (Figure 12). Source of X-ray was Cu k-alpha and measurements were made at room temperature with a wavelength of 1.5406 Å, step intervals of 0.04 in 2Θ between 30° and 100° and speed of 1 s/step. XRD spectrum was analyzed on the standard reference planes for fabricated samples. It was possible to obtain different phases and texture types of crystal structures.

Figure 12. Bruker D8 Advance X-ray diffractometer.

3.8. Hardness Analysis

A Vickers hardness test was conducted on the samples using the LECO LM 300 AT Micro Hardness Tester (ST Joesph, MI). The applied load was 500 g force for 10s. Three indentations were done, and the average measured hardness was reported. (See Figure 13)

Figure 13. LECO LM 300 AT Micro Hardness Tester.

3.9. Finite Element Analysis

To estimate and visualize the local strains in the isotropic lattice structures as well as TPMS, FE analysis was conducted. To this aim, the designed porous parts were imported into Altair Hypermesh (© 2020 Altair Engineering, Inc, USA), and the tetragonal mesh was created. Material properties of Inconel 718 alloy (Modulus of Elasticity E=160 GPa, Poisson's ratio v=0.294) were then assigned to all elements in the mesh. Next, the parts were deformed up to a global displacement of 1 mm. Finally, the local strains formed on the pore walls were analyzed.

Chapter 4. Results and Discussion

4.1 Fabricated samples

Figure 14 represents the SLM fabricated porous Inconel 718 parts with the constant porosity level of 45 %, but varying porosity types of BCC, BCC-Z, FCC, FCC-Z, Schwartz, Gyroid, and Diamond. These parts were fabricated on top of a Stainless-Steel build plate.

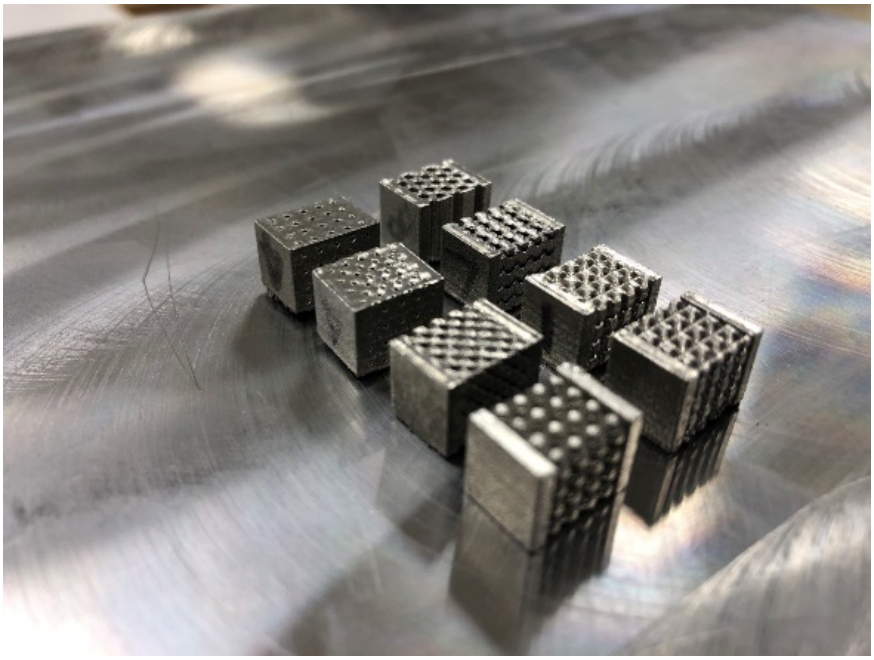

Figure 14. Selective laser melted Inconel 718 specimens created with different porosity types: BCC, BCC-Z, FCC, FCC-Z, Gyroid, Schwartz, Diamond.

4.2. Mechanical Testing

Figure 15 represents the stress-strain graphs of compression tests on the as-fabricated BCC, BCC-Z, FCC, FCC-Z, Gyroid, Diamond, and Schwartz porous specimens having the same level of porosity of 45%. It can be seen that the porosity type had a direct effect on the maximum force. Gyroid-type demonstrated the maximum elongation at failure (4.8 mm), which was slightly higher than what was seen in the Diamond-type (4.1 mm) and at least seven times more than what seen in the Schwarz-type (0.81 mm) or BCC-type (0.81 mm). It should be noted that Gyroid-type and Diamond-type did not fail after applying 83 KN force, however, the testing was stopped due to the defined load limit for the testing machine. While

showing the highest elongation and strength at failure, Gyroid-type showed low yield stress and a lowest modulus of elasticity, when compared with other types of porosity. Whereas diamond had lowest yield stress but higher modulus of elasticity than gyroid and Schwartz. Amongst lattice structures, BCC-type and FCC-type demonstrated the highest equivalent modulus of elasticity. BCC-type demonstrated lower strength, but higher modulus of elasticity, when compared with BCC-Z type. In a similar manner, FCC-type demonstrated lower strength, but higher modulus of elasticity, when compared with FCC-Z type. This can be explained by the fact that FCC-Z and BCC-Z have Z-pillar in the same direction of the compression loading, but smaller strut size, which in turn increase their strength and decrease their modulus of elasticity, respectively and elongation at failure of porous Inconel 718 samples. The failure stress was found to be maximum for FCC and minimum for BCC.

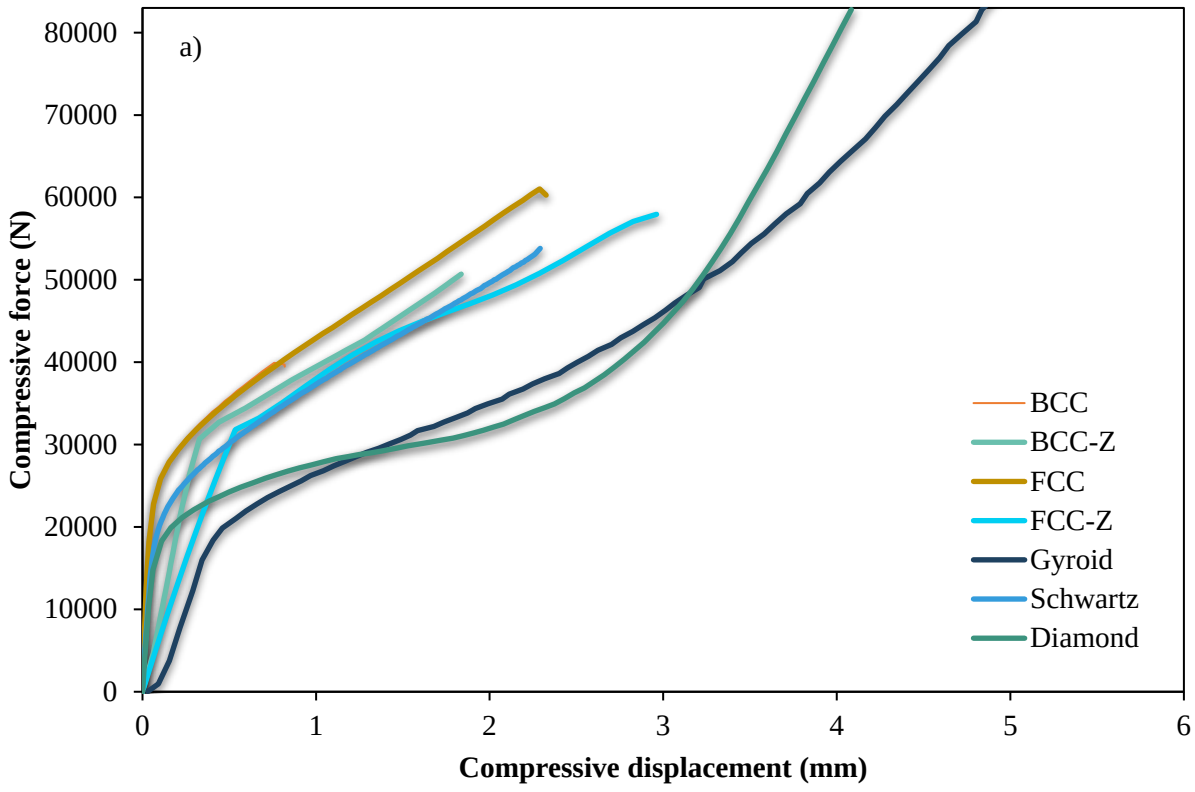

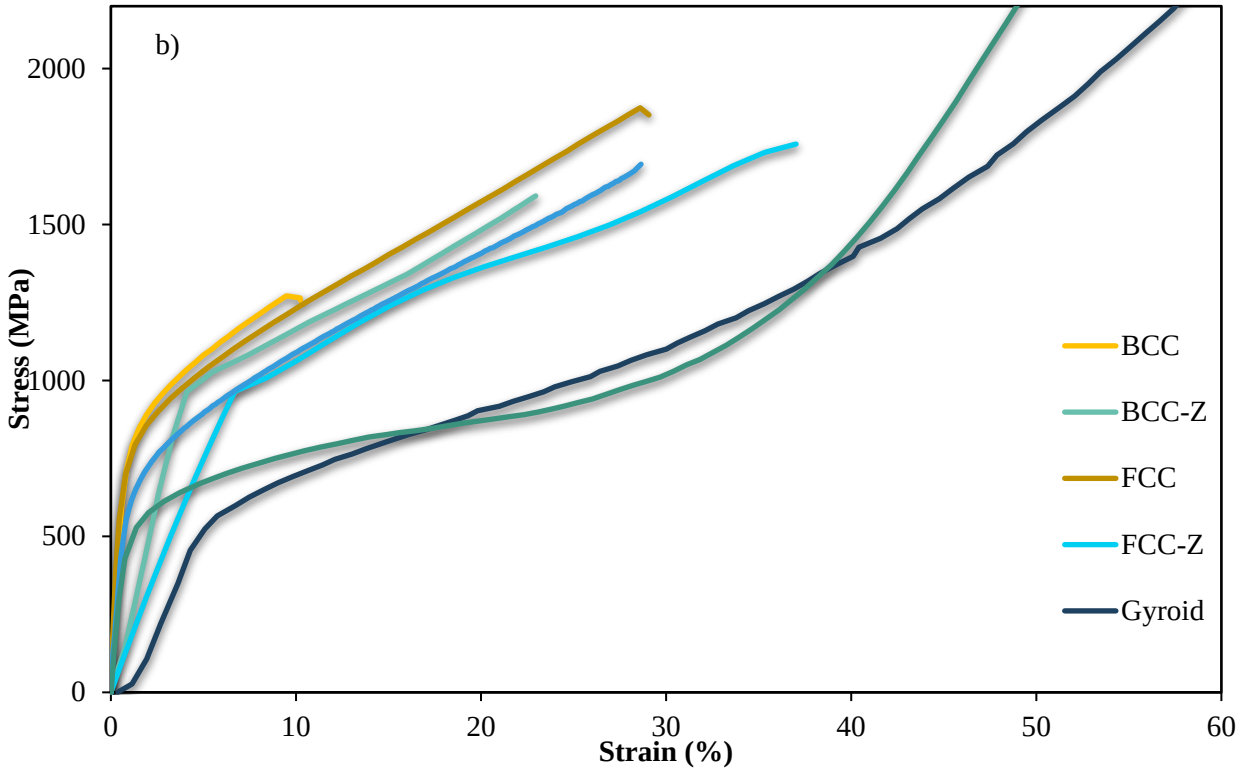

Figure 15. (a) Load-displacement, and (b) stress-strain curve for the porous parts with different porosity shape.

With the same level of porosity, Table 5 reports the equivalent modulus of elasticity (MPa), yield stress (MPa), stress at failure (MPa), and strain at failure (%). To calculate these values, the average initial cross-section area of the porous structures was used, and load-displacement graphs were converted into stress-strain plots.

Table 4. The modulus of elasticity, yield stress, stress at failure, and the strain at failure for BCC, BCC-Z, FCC, FCC-Z, Gyroid, Schwartz, and Diamond.

Porosity Type	Modulus of Elasticity (MPa)	Yield Stress (MPa)	Failure Stress (KN)	Failure Strain (mm/mm)
BCC	116	719	39.7	0.10
BCC-Z	18	946	50.6	0.22
FCC	129	558	61.2	0.28
FCC-Z	15	965	57.9	0.37
Gyroid	7	523	-	-

Schwartz	96	526	53.8	0.28
Diamond	75	428	-	-

The structure of the tested parts was further observed to investigate the failure mechanisms of the porous structures. As can be seen in Figure 16, amongst TPMS structures, Gyroid-type demonstrated the highest level of deformation while Schwartz-type showed a relatively low level of distortion. This could be attributed to the fact that Schwartz-type had decreased the size of the struts when compared with the other two types. Gyroid-type and Diamond-type relatively showed higher deformation in comparison with the lattice structures, such as BCC or FCC-Z. Also, FCC-Z demonstrated slightly lower deformation when compared with BCC due to the added z-pillar. Further interpretation from Table 4 shows the difference between the modulus of elasticity values that is found high for BCC and low for BCC- Z. This happens due to reduction in the diameter of the struts present in BCC-Z to accommodate for same 45% porosity thereby dropping the modulus of elasticity values to a greater extent. This is also found in FCC-Z that behaves similarly to BCC-Z.

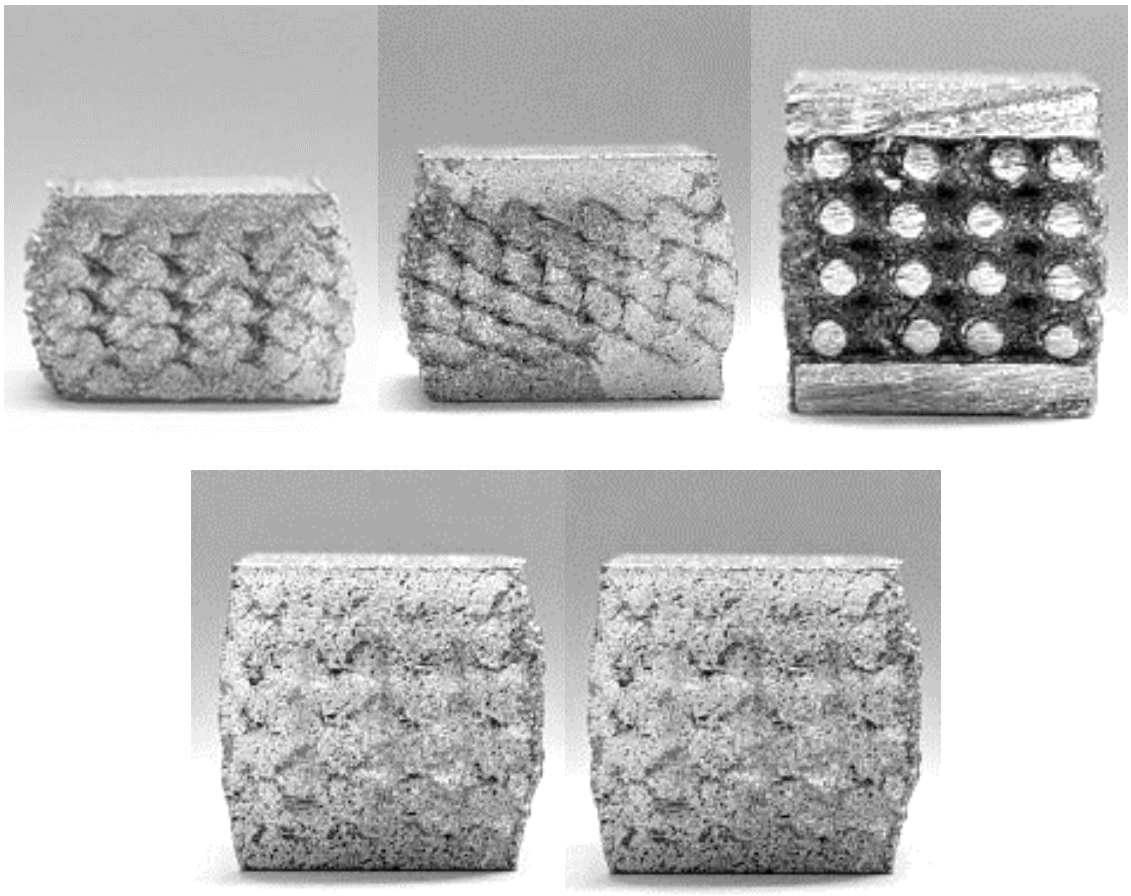

Figure 16. The structure of the porous parts after the compression testing until failure: a) Gyroid-type, b) Diamond-type, c) Schwartz-type, d) FCC-Z, e) BCC.

4.3. Microstructure Analysis

To further look into different patterns for the failure of the porous samples, microstructure analysis was carried out on the powder, as-fabricated specimens, as well as the fabricated parts. The SEM image of powder shown in Figure 17a reveals that the powder had acceptable particle size, spherical shape, good flowability and packing density, low impurity content, and excellent transformation ability. The distribution of the new powder particle sizes was analyzed using ImageJ "Analyze Particles" function, and the results are presented in Figure 17b. The average particle size of fresh Inconel 718 powder was 18 µm. Therefore, it was inferred that the employed powder was not the reason for the premature-failure of some of the samples.

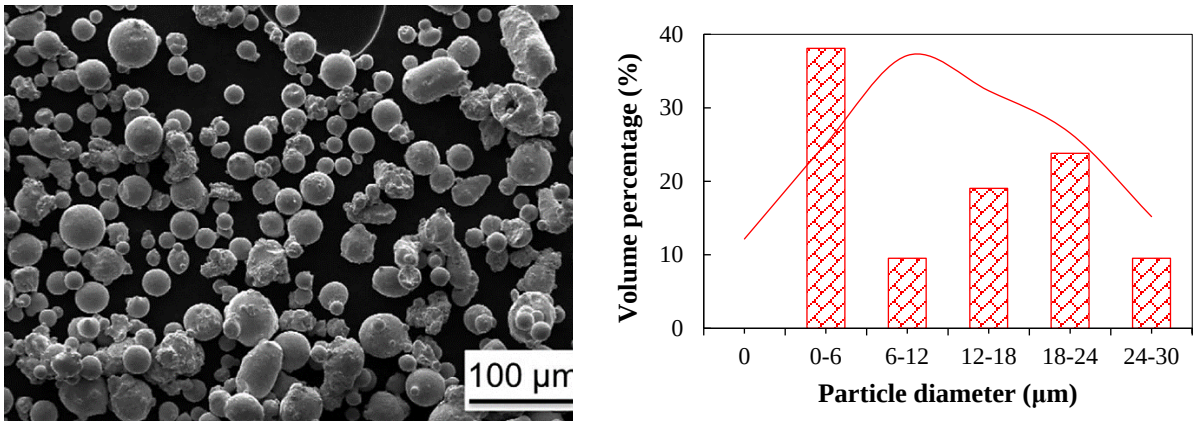

Figure 17. (a) SEM micrograph and (b) powder size distribution for commercial EOS Inconel 718 powder (right).

The SEM image of fabricated BCC, BCC-Z, FCC, FCC-Z, Schwartz, Gyroid, Diamond samples is presented in Figure 18. Examination surfaces of all the fabricated unit cells revealed the presence of regions of numerous unmelted and partially melted powders on the external surfaces of the struts, shown as circles in Figure 18a-g. Such areas could raise local stress and eventually lead to crack initiation during mechanical testing. These types of defects are expected to decrease the mechanical strength and be the leading cause for a premature fracture of all the fabricated parts. The struts, however, were observed to be sufficiently dense confirms that the main struts are fully melted. Amongst all the samples, Gyroid-type demonstrated the lowest amount of surface defects, which was expected because this specimen showed the most moderate elongation and tolerable force at failure.

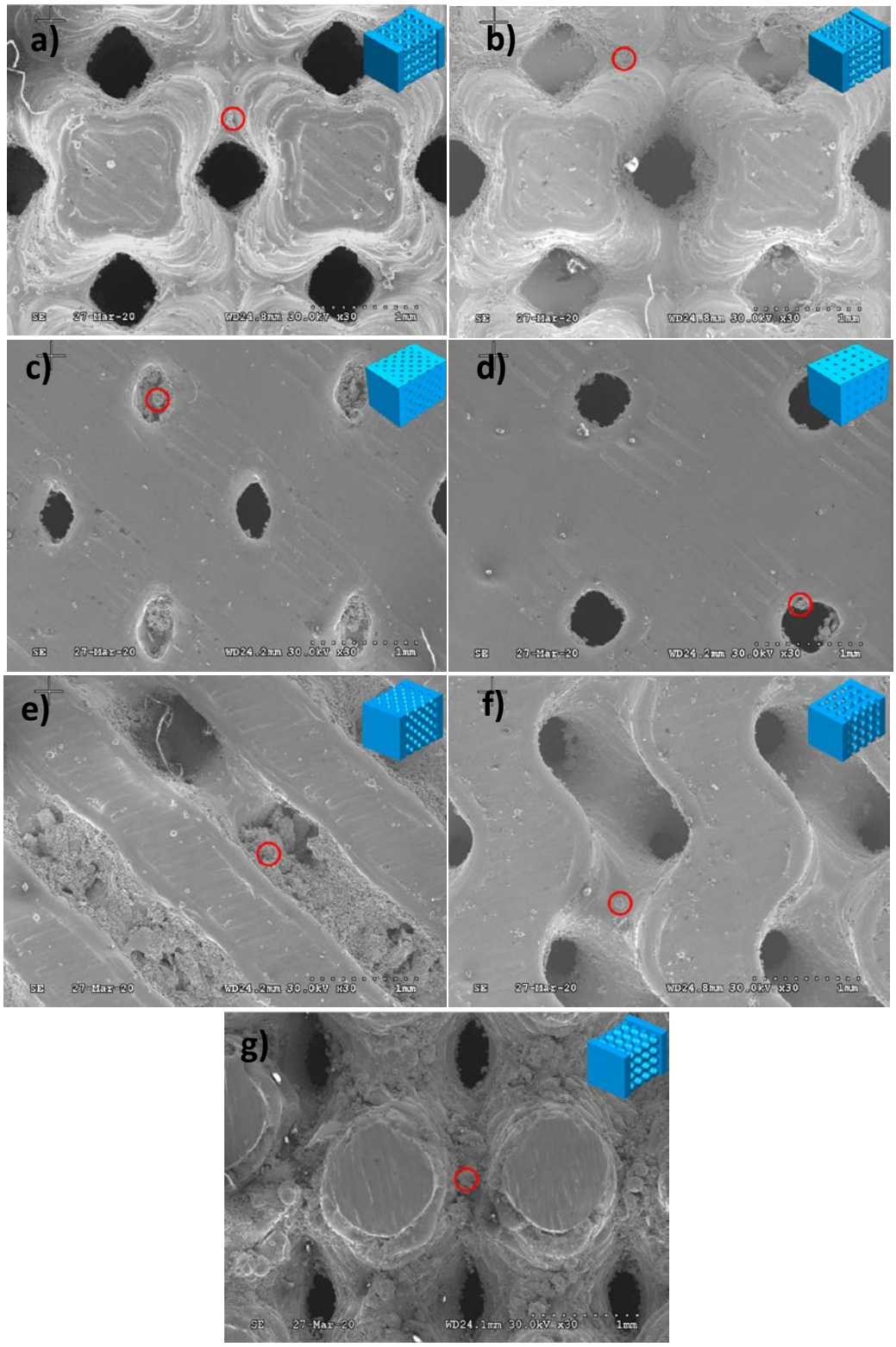

Figure 18. SEM images of a) BCC; b) BCC-Z; c) FCC; d) FCC-Z; e) Diamond; f) Gyroid; g) Schwartz parts with 45% porosity. Examination surfaces of all the fabricated unit cells revealed the presence of regions of numerous unmelted and partially melted powders on the external surfaces of the struts.

To check the uniformity of the microstructure of the fabricated samples, SEM images of three different regions along the height were generated and represented in Figure 19. It can be seen that the melt pools have an average depth of 70 µm in all the three zones along the building direction, i.e., near the substrate, middle region, and the area near the top surface of the fabricated samples. It can be inferred that the microstructure was almost uniform along the build direction.

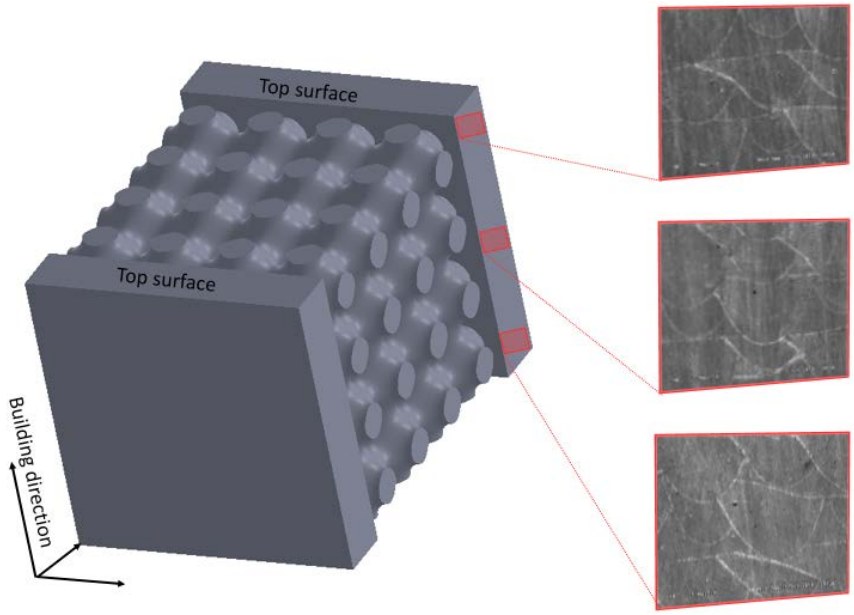

Figure 19. SEM micrograph of Side view of melt pools formed in SLM fabricated parts reveals that the size

4.4. Compositional Analysis

Figure 20 represents the XRD graphs for the employed powder and the SLM fabricated parts. Major peaks were observed at 43°, 51°, 74°, 91°, and 96° for both fresh powder and the SLM parts. The phases were recognized to be γ, γ', γ" and δ. As reported in The quantity of the phases existed in fresh powder was different from that of the fabricated components, as indicated in Table 5, the γ, γ' and γ" phases were found to be 71.15 %, 12.29 %, 16.55 %, respectively in the fabricated part. In contrast, they were 74.45%, 19.64% and 5.89% in the fresh powder respectively. It was found that the γ" in the fabricated parts was higher than that observed in the powder whereas γ' value was lower in the fabricated part than fresh powder. γ" is an

essential phase of Inconel 718, which is also known as the strengthening phase and profoundly influences the mechanical properties of the fabricated sample.

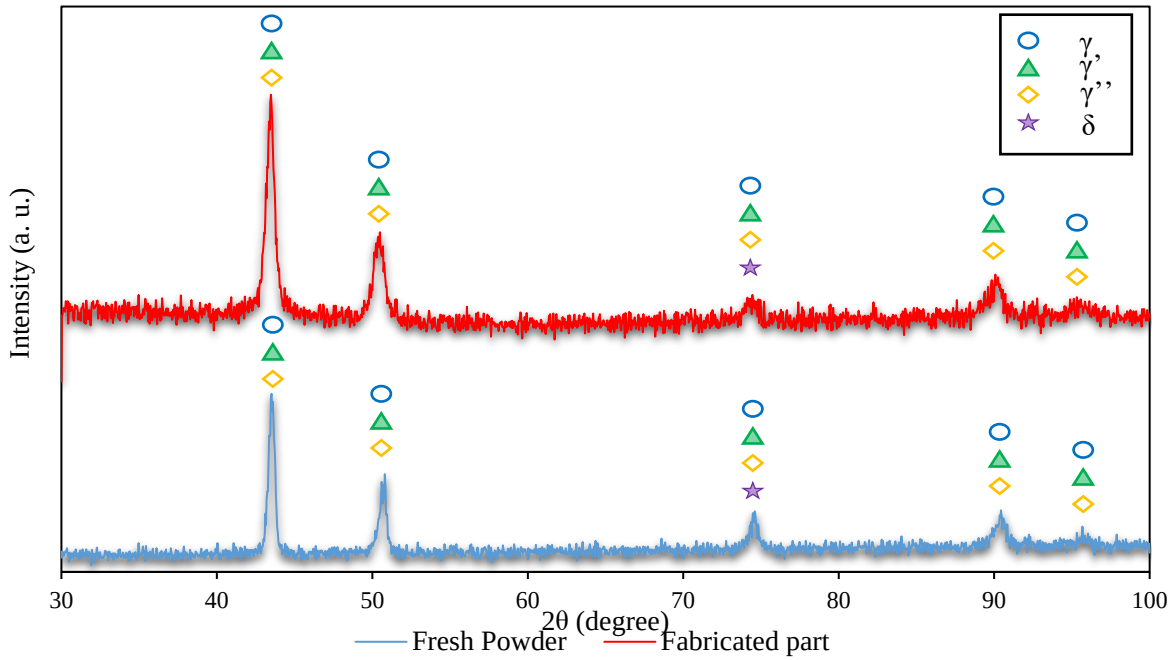

Figure 20. XRD graphs showing the different phases in the IN718 powder and fabricated sample.

Table 5. Calculation of Phase area % for the fabricated Inconel 718 sample on top of different support structures.

	Peak	Phase area (%)		
		γ	γ'	γ''
Fresh powder	1	70.6	29.39	0
	2	74.45	19.64	5.89
	3	100	0	0
Fabricated sample	1	75.4	21.7	2.9
	2	73.1	14.1	12.8
	3	72.7	16.2	11.1

4.5. Finite Element Analysis

Under same level of loading, the local strains of the lattice structures were found to be maximum in BCC after compression loading conducted in FEA tool (Figure 21). BCC-Z exhibited relatively lower local strains when compared with BCC. This observation essentially confirms the weaker properties observed in BCC lattice structure (See Figure 15). Similarly, FCC-Z showed lower strains than FCC. Overall FCC/ FCC-Z strain values were less compared to that of BCC and BCC-Z for exact loading values. The significance of lattice structure type can be found here by the observed variation in the strain values even though the loading and dimensions were same.

a

b

c

c

d

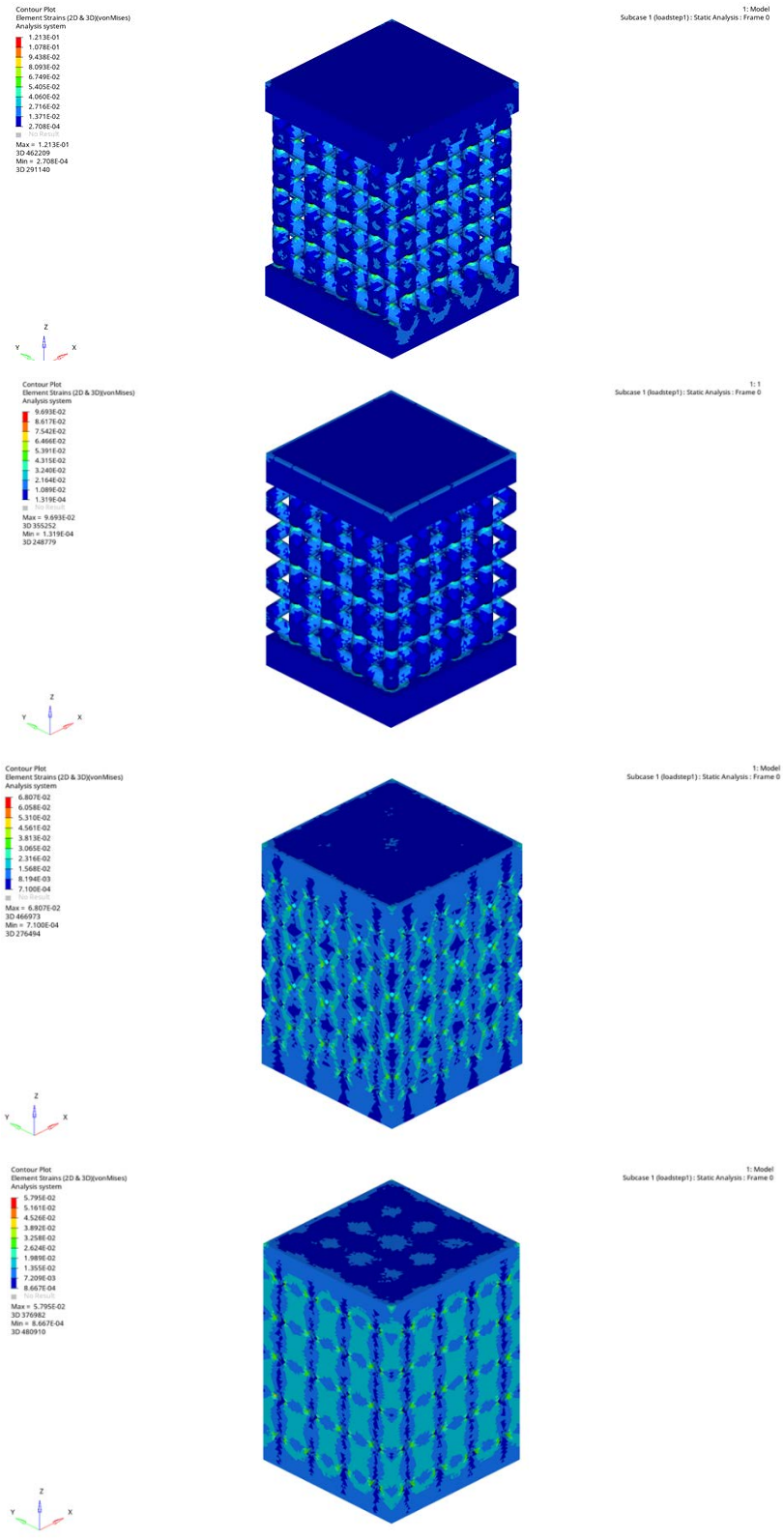

Figure 21. Strain distribution resulting from a constant distributed load over the top plate for different porous structures: a) BCC; b) BCC-Z; c) FCC; d) FCC-Z; e) Gyroid; f) Schwartz; g) Diamond.

Chapter 5. Conclusions and Future Works

5.1. Conclusion

SLM and its ability to fabricate complex lattice structures has opened opportunities for various research works. In this paper, the efforts made to study about the lattices (BCC, BCC-Z, FCC, FCC-Z) and triply periodic minimal surfaces (Gyroid, Schwartz, Diamond). To this aim, the mechanical, microstructural, and compositional properties of these structures have been discussed. It was found that the porosity type had a direct effect on the maximum strength, maximum strain, and modulus of elasticity. Gyroid-type exhibited the lowest modulus of elasticity while showing the highest elongation and strength at failure. BCC-type and FCC-type demonstrated high modulus of elasticity and low strength when compared with their corresponding Z types (FCC-Z and BCC-Z had higher strength and lower modulus of elasticity). This can be explained by the fact that FCC-Z and BCC-Z have Z-pillar in the same direction of the compression loading, but smaller strut size, which in turn increase their strength and decrease their modulus of elasticity, respectively. From the microstructure analysis the powder had acceptable particle size, spherical shape, good flowability and packing density, low impurity content, and excellent transformation ability. It was inferred that the employed powder was not the reason for the premature failure of some of the samples. The presence of regions of numerous unmelted and partially melted powders on the external surfaces of the struts present in the samples could raise local stress and eventually lead to crack initiation during mechanical testing. These types of defects are expected to decrease the mechanical strength leading to a premature fracture of all the fabricated parts. Gyroid-type demonstrated the lowest amount of surface defects, which was expected because this specimen showed the most moderate elongation and tolerable force at failure. From the compositional analysis, γ” in the fabricated parts was higher than that observed in the powder which is the strengthening phase and profoundly influences the mechanical properties of the fabricated sample.

5.2. Future Work

While this study has generated a set results from mechanical and microstructural point of view, there is still scope for analyzing melt pools, grain formation, and defects within the struts. Further scope lies in evaluating fatigue properties of these parts and obtain microstructure-property relationship.

References

[1] M. Smith, Z. Guan, W. Cantwell, Finite element modelling of the compressive response of lattice structures manufactured using the selective laser melting technique, International Journal of Mechanical Sciences 67 (2013) 28-41.
[2] Y. Liu, X. Li, L.C. Zhang, T. Sercombe, Processing and properties of topologically optimised biomedical Ti–24Nb–4Zr–8Sn scaffolds manufactured by selective laser melting, Materials Science and Engineering: A 642 (2015) 268-278.
[3] R.C. Reed, The superalloys: fundamentals and applications, Cambridge university press2008.
[4] D.F. Paulonis, J.J. Schirra, Alloy 718 at Pratt & Whitney-Historical perspective and future challenges, Superalloys 718(625,706) (2001) 13-23.
[5] T.R. Newton, S.N. Melkote, T.R. Watkins, R.M. Trejo, L. Reister, Investigation of the effect of process parameters on the formation and characteristics of recast layer in wire-EDM of Inconel 718, Materials Science and Engineering: A 513 (2009) 208-215.
[6] A. Iturbe, E. Giraud, E. Hormaetxe, A. Garay, G. Germain, K. Ostolaza, P.J. Arrazola, Mechanical characterization and modelling of Inconel 718 material behavior for machining process assessment, Materials Science and Engineering: A 682 (2017) 441-453.
[7] B. Geddes, H. Leon, X. Huang, Superalloys: alloying and performance, Asm International2010.
[8] L. Garimella, P. Liaw, D. Klarstrom, Fatigue behavior in nickel-based superalloys: A literature review, Jom 49(7) (1997) 67.
[9] B. Pieraggi, J. Uginet, Fatigue and creep properties in relation with alloy 718 microstructure, Superalloys 718 (1994) 625-706.
[10] H. Eiselstein, D. Tillack, The invention and definition of alloy 625, Superalloys 718(625) (1991) 1-14.
[11] J. Brooks, P. Bridges, Metallurgical stability of Inconel alloy 718, Superalloys 88 (1988) 33-42.
[12] Y.-T. Chen, A.-C. Yeh, M.-Y. Li, S.-M. Kuo, Effects of processing routes on room temperature tensile strength and elongation for Inconel 718, Materials & Design 119 (2017) 235-243.
[13] W.M. Tucho, P. Cuvillier, A. Sjolyst-Kverneland, V. Hansen, Microstructure and hardness studies of Inconel 718 manufactured by selective laser melting before and after solution heat treatment, Materials Science and Engineering: A 689 (2017) 220-232.
[14] M. Okasha, P. Mativenga, N. Driver, L. Li, Sequential laser and mechanical micro-drilling of Ni superalloy for aerospace application, CIRP annals 59(1) (2010) 199-202.
[15] D. Aspinwall, S. Soo, A. Berrisford, G. Walder, Workpiece surface roughness and integrity after WEDM of Ti–6Al–4V and Inconel 718 using minimum damage generator technology, CIRP annals 57(1) (2008) 187-190.
[16] R. Li, M. Yao, W. Liu, X. He, Isolation and determination for δ, γ′ and γ ″phases in Inconel 718 alloy, Scripta materialia 46(9) (2002) 635-638.
[17] S. Azadian, L.-Y. Wei, R. Warren, Delta phase precipitation in Inconel 718, Materials characterization 53(1) (2004) 7-16.
[18] C.A. Borg, R.W. Hatala, J.J. Schirra, Characterization of vacuum die cast Inconel 718 and derivatives (PWA 1472/PWA 1473), Superalloys 718, 625, 706 and Various Derivatives (2001) 627-636.
[19] H. Fecht, D. Furrer, Processing of Nickel-Base Superalloys for Turbine Engine Disc Applications, Advanced engineering materials 2(12) (2000) 777-787.
[20] S. Semiatin, K. McClary, A. Rollett, C. Roberts, E. Payton, F. Zhang, T. Gabb, Microstructure evolution during supersolvus heat treatment of a powder metallurgy nickel-base superalloy, Metallurgical and Materials Transactions A 43(5) (2012) 1649-1661.
[21] L. Chang, W. Sun, Y. Cui, R. Yang, Preparation of hot-isostatic-pressed powder metallurgy superalloy Inconel 718 free of prior particle boundaries, Materials Science and Engineering: A 682 (2017) 341-344.
[22] S. Saedi, S.E. Saghaian, A. Jahadakbar, N.S. Moghaddam, M.T. Andani, S.M. Saghaian, Y.C. Lu, M. Elahinia, H.E. Karaca, Shape memory response of porous NiTi shape memory alloys fabricated by selective laser melting, Journal of Materials Science: Materials in Medicine 29(4) (2018) 40.

[23] S. Saghaian, A. Amerinatanzi, N. Moghaddam, A. Majumdar, M. Nematollahi, S. Saedi, M. Elahinia, H. Karaca, Mechanical and shape memory properties of triply periodic minimal surface (TPMS) NiTi structures fabricated by selective laser melting, Biology, Engineering and Medicine. (2018).
[24] N. Shayesteh Moghaddam, Toward patient specific long lasting metallic implants for mandibular segmental defects, University of Toledo, 2015.
[25] N. Shayesteh Moghaddam, D. Dean, M. Miller, M. Elahinia, Improving bone implant success by using nitinol as a substitute for titanium: A modeling comparison, Proceedings of the ASME, 2014.
[26] S. Srivathsan, B.B. Ravichander, N.S. Moghaddam, N. Swails, A. Amerinatanzi, Investigation of the strength of different porous lattice structures manufactured using selective laser melting, Behavior and Mechanics of Multifunctional Materials IX, International Society for Optics and Photonics, 2020, p. 113771B.
[27] S. Thakare, B.B. Ravichander, N. Swails, N.S. Moghaddam, A. Amerinatanzi, The effect of support structure geometry on surface topography of selectively laser melted parts, Behavior and Mechanics of Multifunctional Materials IX, International Society for Optics and Photonics, 2020, p. 113771D.
[28] A. Amerinatanzi, N. Shayesteh Moghaddam, H. Ibrahim, M. Elahinia, Evaluating a NiTi implant under realistic loads: A simulation study, ASME 2016 Conference on Smart Materials, Adaptive Structures and Intelligent Systems, American Society of Mechanical Engineers Digital Collection, 2016.
[29] A. Amerinatanzi, N. Shayesteh Moghaddam, H. Ibrahim, M. Elahinia, The effect of porosity type on the mechanical performance of porous niti bone implants, ASME 2016 Conference on Smart Materials, Adaptive Structures and Intelligent Systems, American Society of Mechanical Engineers Digital Collection, 2016.
[30] A. Amerinatanzi, N. Shayesteh Moghaddam, A. Jahadakbar, D. Dean, M. Elahinia, On the effect of screw preload on the stress distribution of mandibles during segmental defect treatment using an additively manufactured hardware, ASME 2016 11th international manufacturing science and engineering conference, American Society of Mechanical Engineers Digital Collection, 2016.
[31] A. Amerinatanzi, H. Zamanian, N. Shayesteh Moghaddam, H. Ibrahim, M.S. Hefzy, M. Elahinia, On the advantages of superelastic Niti in ankle foot orthoses, ASME 2016 Conference on Smart Materials, Adaptive Structures and Intelligent Systems, American Society of Mechanical Engineers Digital Collection, 2016.
[32] A. Amerinatanzi, H. Zamanian, N. Shayesteh Moghaddam, A. Jahadakbar, M. Elahinia, Application of the Superelastic NiTi Spring in Ankle Foot Orthosis (AFO) to Create Normal Ankle Joint Behavior, Bioengineering 4(4) (2017) 95.
[33] M.J. Ashrafi, A. Amerinatanzi, Z. Saebi, N.S. Moghaddam, R. Mehrabi, H. Karaca, M. Elahinia, Shape memory response of cellular lattice structures: Unit cell finite element prediction, Mechanics of Materials 125 (2018) 26-34.
[34] I. Gibson, D.W. Rosen, B. Stucker, Design for additive manufacturing, Additive Manufacturing Technologies, Springer2010, pp. 299-332.
[35] H.D. Dean, M.H. Elahinia, C. Haberland, M.J. Miller, A. Sutradhar, N.S. Moghaddam, J.M. Walker, R. Skoracki, Methods, devices, and manufacture of the devices for musculoskeletal reconstructive surgery, US Patent App. 15/124,660, 2017.
[36] A. Dehghanghadikolaei, H. Ibrahim, A. Amerinatanzi, M. Hashemi, N.S. Moghaddam, M. Elahinia, Improving corrosion resistance of additively manufactured nickel–titanium biomedical devices by micro-arc oxidation process, Journal of materials science 54(9) (2019) 7333-7355.
[37] M. Elahinia, N.S. Moghaddam, A. Amerinatanzi, S. Saedi, G.P. Toker, H. Karaca, G.S. Bigelow, O. Benafan, Additive manufacturing of NiTiHf high temperature shape memory alloy, Scripta Materialia 145 (2018) 90-94.
[38] M. Elahinia, N.S. Moghaddam, M.T. Andani, A. Amerinatanzi, B.A. Bimber, R.F. Hamilton, Fabrication of NiTi through additive manufacturing: A review, Progress in Materials Science 83 (2016) 630-663.

[39] B. Farhang, B.B. Ravichander, F. Venturi, A. Amerinatanzi, N.S. Moghaddam, Study on variations of microstructure and metallurgical properties in various heat-affected zones of SLM fabricated Nickel–Titanium alloy, Materials Science and Engineering: A (2020) 138919.
[40] A. Hadi, M. Qasemi, M. Elahinia, N. Moghaddam, Modeling and experiment of a flexible module actuated by shape memory alloy wire, ASME 2014 Conference on Smart Materials, Adaptive Structures and Intelligent Systems, American Society of Mechanical Engineers Digital Collection, 2014.
[41] H. Ibrahim, A. Jahadakbar, A. Dehghan, N.S. Moghaddam, A. Amerinatanzi, M. Elahinia, In Vitro Corrosion Assessment of Additively Manufactured Porous NiTi Structures for Bone Fixation Applications, Metals 8(3) (2018) 164.
[42] H. Ibrahim, N. Moghaddam, M. Elahinia, Mechanical and in vitro corrosion properties of a heat-treated Mg-Zn-Ca-Mn alloy as a potential bioresorbable material, Advances in Metallurgical and Material Engineering 1(1) (2017).
[43] K. Mamidi, H.K. Talla, B.B. Ravichander, B. Farhang, N.S. Moghaddam, A. Amerinatanzi, Study on the influence of post-processing parameters over microstructure and metallurgical properties of NiTi alloy, Behavior and Mechanics of Multifunctional Materials IX, International Society for Optics and Photonics, 2020, p. 113770V.
[44] N. Moghaddam, A. Amerinatanzi, S. Saedi, A. Turabi, H. Karaca, M. Elahinia, Stiffness Tuning of Niti Implants Through Aging, Proceedings of the ASME 2016 Conference on Smart Materials, Adaptive Structures and Intelligent Systems, Stowe, VT, USA, 2016, pp. 28-30.
[45] N.S. Moghaddam, A. Amerinatanzi, S. Saedi, A.S. Turabi, H. Karaca, M. Elahinia, SMASIS2016-9289.
[46] N.S. Moghaddam, M. Elahinia, M. Miller, D. Dean, Enhancement of bone implants by substituting nitinol for titanium (Ti-6Al-4V): A modeling comparison, ASME 2014 conference on smart materials, adaptive structures and intelligent systems, American Society of Mechanical Engineers Digital Collection, 2014.
[47] N.S. Moghaddam, S. Saedi, A. Amerinatanzi, A. Hinojos, A. Ramazani, J. Kundin, M.J. Mills, H. Karaca, M. Elahinia, Achieving superelasticity in additively manufactured NiTi in compression without post-process heat treatment, Scientific reports 9(1) (2019) 1-11.
[48] N.S. Moghaddam, S. Saedi, A. Amerinatanzi, A. Jahadakbar, E. Saghaian, H. Karaca, M. Elahinia, Influence of SLM on compressive response of NiTi scaffolds, Behavior and Mechanics of Multifunctional Materials and Composites XII, International Society for Optics and Photonics, 2018, p. 105960H.
[49] N.S. Moghaddam, S. Saedi, A. Amerinatanzi, E. Saghaian, A. Jahadakbar, H. Karaca, M. Elahinia, Selective laser melting of Ni-rich NiTi: selection of process parameters and the superelastic response, Behavior and Mechanics of Multifunctional Materials and Composites XII, International Society for Optics and Photonics, 2018, p. 105960W.
[50] N.S. Moghaddam, S.E. Saghaian, A. Amerinatanzi, H. Ibrahim, P. Li, G.P. Toker, H.E. Karaca, M. Elahinia, Anisotropic tensile and actuation properties of NiTi fabricated with selective laser melting, Materials Science and Engineering: A 724 (2018) 220-230.
[51] N.S. Moghaddam, R. Skoracki, M. Miller, M. Elahinia, D. Dean, Three dimensional printing of stiffness-tuned, nitinol skeletal fixation hardware with an example of mandibular segmental defect repair, Procedia CIRP 49 (2016) 45-50.
[52] B.B. Ravichander, B. Farhang, N. Swails, A. Amerinatanzi, N.S. Moghaddam, Analysis of the deviation in properties of selective laser melted samples fabricated by varying process parameters, Behavior and Mechanics of Multifunctional Materials IX, International Society for Optics and Photonics, 2020, p. 113771A.
[53] S. Saedi, N.S. Moghaddam, A. Amerinatanzi, M. Elahinia, H.E. Karaca, On the effects of selective laser melting process parameters on microstructure and thermomechanical response of Ni-rich NiTi, Acta Materialia 144 (2018) 552-560.
[54] L. Ardila, F. Garciandia, J. González-Díaz, P. Álvarez, A. Echeverria, M. Petite, R. Deffley, J. Ochoa, Effect of IN718 recycled powder reuse on properties of parts manufactured by means of Selective Laser Melting, Physics Procedia 56 (2014) 99-107.

[55] C. Yan, L. Hao, A. Hussein, D. Raymont, Evaluations of cellular lattice structures manufactured using selective laser melting, International Journal of Machine Tools and Manufacture 62 (2012) 32-38.
[56] C. Haase, J. Bültmann, J. Hof, S. Ziegler, S. Bremen, C. Hinke, A. Schwedt, U. Prahl, W. Bleck, Exploiting process-related advantages of selective laser melting for the production of high-manganese steel, Materials 10(1) (2017) 56.
[57] C. Tan, K. Zhou, W. Ma, B. Attard, P. Zhang, T. Kuang, Selective laser melting of high-performance pure tungsten: parameter design, densification behavior and mechanical properties, Science and Technology of advanced MaTerialS 19(1) (2018) 370-380.
[58] M. Shellabear, O. Nyrhilä, DMLS-Development history and state of the art, Laser Assisted Netshape engineering 4, proceedings of the 4th LANE (2004) 21-24.
[59] Iamchaitanya, SLM, [https://iamchaitanya.wordpress.com/2015/07/22/powder-metallurgy/]done

. Iamchaitanya, Website, 2020.
[60] J.-P. Kruth, P. Mercelis, J.V. Vaerenbergh, L. Froyen, M. Rombouts, Binding mechanisms in selective laser sintering and selective laser melting, Rapid prototyping journal 11(1) (2005) 26-36.
[61] B. Xiao, Y. Zhang, Numerical simulation of direct metal laser sintering of single-component powder on top of sintered layers, Journal of manufacturing science and engineering 130(4) (2008).
[62] Q. Jia, D. Gu, Selective laser melting additive manufactured Inconel 718 superalloy parts: high-temperature oxidation property and its mechanisms, Optics & Laser Technology 62 (2014) 161-171.
[63] N. Raghavan, R. Dehoff, S. Pannala, S. Simunovic, M. Kirka, J. Turner, N. Carlson, S.S. Babu, Numerical modeling of heat-transfer and the influence of process parameters on tailoring the grain morphology of IN718 in electron beam additive manufacturing, Acta Materialia 112 (2016) 303-314.
[64] W. Tillmann, C. Schaak, J. Nellesen, M. Schaper, M. Aydinöz, K.-P. Hoyer, Hot isostatic pressing of IN718 components manufactured by selective laser melting, Additive Manufacturing 13 (2017) 93-102.
[65] C. Körner, H. Helmer, A. Bauereiß, R.F. Singer, Tailoring the grain structure of IN718 during selective electron beam melting, MATEC Web of Conferences, EDP Sciences, 2014, p. 08001.
[66] A. Hinojos, J. Mireles, A. Reichardt, P. Frigola, P. Hosemann, L.E. Murr, R.B. Wicker, Joining of Inconel 718 and 316 Stainless Steel using electron beam melting additive manufacturing technology, Materials & Design 94 (2016) 17-27.
[67] D.M. Lambert, IN718 additive manufacturing properties and influences, (2015).
[68] Y. Zhang, X. Cao, P. Wanjara, M. Medraj, Oxide films in laser additive manufactured Inconel 718, Acta materialia 61(17) (2013) 6562-6576.
[69] V. Popovich, E. Borisov, A. Popovich, V.S. Sufiiarov, D. Masaylo, L. Alzina, Functionally graded Inconel 718 processed by additive manufacturing: Crystallographic texture, anisotropy of microstructure and mechanical properties, Materials & Design 114 (2017) 441-449.
[70] Y. Tian, D. McAllister, H. Colijn, M. Mills, D. Farson, M. Nordin, S. Babu, Rationalization of microstructure heterogeneity in INCONEL 718 builds made by the direct laser additive manufacturing process, Metallurgical and Materials Transactions A 45(10) (2014) 4470-4483.
[71] K. Moussaoui, W. Rubio, M. Mousseigne, T. Sultan, F. Rezai, Effects of Selective Laser Melting additive manufacturing parameters of Inconel 718 on porosity, microstructure and mechanical properties, Materials Science and Engineering: A 735 (2018) 182-190.
[72] K. Amato, S. Gaytan, L. Murr, E. Martinez, P. Shindo, J. Hernandez, S. Collins, F. Medina, Microstructures and mechanical behavior of Inconel 718 fabricated by selective laser melting, Acta Materialia 60(5) (2012) 2229-2239.
[73] J. Shi, L. Zhu, L. Li, Z. Li, J. Yang, X. Wang, A TPMS-based method for modeling porous scaffolds for bionic bone tissue engineering, Scientific reports 8(1) (2018) 1-10.
[74] H. Nakajima, Fabrication, properties and application of porous metals with directional pores, Progress in Materials Science 52(7) (2007) 1091-1173.
[75] C.B. Williams, J.K. Cochran, D.W. Rosen, Additive manufacturing of metallic cellular materials via three-dimensional printing, The International Journal of Advanced Manufacturing Technology 53(1-4) (2011) 231-239.

[76] J. Zhou, P. Shrotriya, W. Soboyejo, On the deformation of aluminum lattice block structures: from struts to structures, Mechanics of materials 36(8) (2004) 723-737.
[77] A. Amerinatanzi, R. Mehrabi, H. Ibrahim, A. Dehghan, N. Shayesteh Moghaddam, M. Elahinia, Predicting the Biodegradation of Magnesium Alloy Implants: Modeling, Parameter Identification, and Validation, Bioengineering 5(4) (2018) 105.
[78] D. Mahmoud, M.A. Elbestawi, Lattice structures and functionally graded materials applications in additive manufacturing of orthopedic implants: a review, Journal of Manufacturing and materials Processing 1(2) (2017) 13.
[79] X. Tan, Y. Kok, Y.J. Tan, G. Vastola, Q.X. Pei, G. Zhang, Y.-W. Zhang, S.B. Tor, K.F. Leong, C.K. Chua, An experimental and simulation study on build thickness dependent microstructure for electron beam melted Ti–6Al–4V, Journal of Alloys and Compounds 646 (2015) 303-309.
[80] M.F. Ashby, L.J. Gibson, Cellular solids: structure and properties, Press Syndicate of the University of Cambridge, Cambridge, UK (1997) 175-231.
[81] M. Mazur, M. Leary, S. Sun, M. Vcelka, D. Shidid, M. Brandt, Deformation and failure behaviour of Ti-6Al-4V lattice structures manufactured by selective laser melting (SLM), The International Journal of Advanced Manufacturing Technology 84(5-8) (2016) 1391-1411.
[82] J.C. Maxwell, L. on the calculation of the equilibrium and stiffness of frames, The London, Edinburgh, and Dublin Philosophical Magazine and Journal of Science 27(182) (1864) 294-299.
[83] K. Ushijima, W. Cantwell, R. Mines, S. Tsopanos, M. Smith, An investigation into the compressive properties of stainless steel micro-lattice structures, Journal of Sandwich Structures & Materials 13(3) (2011) 303-329.
[84] K. Ushijima, W. Cantwell, D. Chen, Prediction of the mechanical properties of micro-lattice structures subjected to multi-axial loading, International Journal of Mechanical Sciences 68 (2013) 47-55.
[85] R. Gümrük, R. Mines, S. Karadeniz, Static mechanical behaviours of stainless steel micro-lattice structures under different loading conditions, Materials Science and Engineering: A 586 (2013) 392-406.
[86] T. Tancogne-Dejean, D. Mohr, Stiffness and specific energy absorption of additively-manufactured metallic BCC metamaterials composed of tapered beams, International Journal of Mechanical Sciences 141 (2018) 101-116.
[87] M. Leary, M. Mazur, J. Elambasseril, M. McMillan, T. Chirent, Y. Sun, M. Qian, M. Easton, M. Brandt, Selective laser melting (SLM) of AlSi12Mg lattice structures, Materials & Design 98 (2016) 344-357.
[88] A. Fogden, S. Hyde, Parametrization of triply periodic minimal surfaces. I. Mathematical basis of the construction algorithm for the regular class, Acta Crystallographica Section A: Foundations of Crystallography 48(4) (1992) 442-451.
[89] Y. Deng, M. Mieczkowski, Three-dimensional periodic cubic membrane structure in the mitochondria of amoebaeChaos carolinensis, Protoplasma 203(1-2) (1998) 16-25.
[90] S. Jiang, A. Göpfert, V. Abetz, Novel morphologies of block copolymer blends via hydrogen bonding, Macromolecules 36(16) (2003) 6171-6177.
[91] J.H. Cartwright, A.L. Mackay, Beyond crystals: the dialectic of materials and information, The Royal Society Publishing, 2012.
[92] H.A. Schwarz, Gesammelte mathematische abhandlungen, American Mathematical Soc.1972.
[93] A.H. Schoen, Infinite periodic minimal surfaces without self-intersections, National Aeronautics and Space Administration1970.
[94] H. Karcher, The triply periodic minimal surfaces of Alan Schoen and their constant mean curvature companions, Manuscripta mathematica 64(3) (1989) 291-357.
[95] H. Karcher, K. Polthier, Construction of triply periodic minimal surfaces, Philosophical Transactions of the Royal Society of London. Series A: Mathematical, Physical and Engineering Sciences 354(1715) (1996) 2077-2104.
[96] D.S. Al-Saedi, S. Masood, M. Faizan-Ur-Rab, A. Alomarah, P. Ponnusamy, Mechanical properties and energy absorption capability of functionally graded F2BCC lattice fabricated by SLM, Materials & Design 144 (2018) 32-44.

[97] M. Mazur, M. Leary, M. McMillan, S. Sun, D. Shidid, M. Brandt, Mechanical properties of Ti6Al4V and AlSi12Mg lattice structures manufactured by Selective Laser Melting (SLM), Laser Additive Manufacturing, Elsevier2017, pp. 119-161.
[98] S.L. Sing, F.E. Wiria, W.Y. Yeong, Selective laser melting of lattice structures: A statistical approach to manufacturability and mechanical behavior, Robotics and Computer-Integrated Manufacturing 49 (2018) 170-180.
[99] R. Wauthle, B. Vrancken, B. Beynaerts, K. Jorissen, J. Schrooten, J.-P. Kruth, J. Van Humbeeck, Effects of build orientation and heat treatment on the microstructure and mechanical properties of selective laser melted Ti6Al4V lattice structures, Additive Manufacturing 5 (2015) 77-84.
[100] I. Maskery, N. Aboulkhair, A. Aremu, C. Tuck, I. Ashcroft, R.D. Wildman, R.J. Hague, A mechanical property evaluation of graded density Al-Si10-Mg lattice structures manufactured by selective laser melting, Materials Science and Engineering: A 670 (2016) 264-274.
[101] M.F. Ashby, R.M. Medalist, The mechanical properties of cellular solids, Metallurgical Transactions A 14(9) (1983) 1755-1769.
[102] R. Hasan, R.A. Mines, E. Shen, S. Tsopanos, W. Cantwell, Comparison on compressive behaviour of aluminium honeycomb and titanium alloy micro lattice blocks, Key Engineering Materials, Trans Tech Publ, 2011, pp. 213-218.
[103] C. Qiu, S. Yue, N.J. Adkins, M. Ward, H. Hassanin, P.D. Lee, P.J. Withers, M.M. Attallah, Influence of processing conditions on strut structure and compressive properties of cellular lattice structures fabricated by selective laser melting, Materials Science and Engineering: A 628 (2015) 188-197.
[104] Z. Xiao, Y. Yang, R. Xiao, Y. Bai, C. Song, D. Wang, Evaluation of topology-optimized lattice structures manufactured via selective laser melting, Materials & Design 143 (2018) 27-37.
[105] H. Gong, K. Rafi, H. Gu, G.J. Ram, T. Starr, B. Stucker, Influence of defects on mechanical properties of Ti–6Al–4 V components produced by selective laser melting and electron beam melting, Materials & Design 86 (2015) 545-554.
[106] T. Maconachie, M. Leary, B. Lozanovski, X. Zhang, M. Qian, O. Faruque, M. Brandt, SLM lattice structures: Properties, performance, applications and challenges, Materials & Design (2019) 108137.
[107] S.Y. Choy, C.-N. Sun, K.F. Leong, J. Wei, Compressive properties of Ti-6Al-4V lattice structures fabricated by selective laser melting: Design, orientation and density, Additive Manufacturing 16 (2017) 213-224.
[108] D. Gu, Y. Shen, Balling phenomena in direct laser sintering of stainless steel powder: Metallurgical mechanisms and control methods, Materials & Design 30(8) (2009) 2903-2910.
[109] M. Santorinaios, W. Brooks, C. Sutcliffe, R. Mines, Crush behaviour of open cellular lattice structures manufactured using selective laser melting, WIT transactions on the built environment 85 (2006).
[110] S. McKown, Y. Shen, W. Brookes, C. Sutcliffe, W. Cantwell, G. Langdon, G. Nurick, M. Theobald, The quasi-static and blast loading response of lattice structures, International Journal of Impact Engineering 35(8) (2008) 795-810.
[111] D.K. Pattanayak, A. Fukuda, T. Matsushita, M. Takemoto, S. Fujibayashi, K. Sasaki, N. Nishida, T. Nakamura, T. Kokubo, Bioactive Ti metal analogous to human cancellous bone: fabrication by selective laser melting and chemical treatments, Acta Biomaterialia 7(3) (2011) 1398-1406.
[112] S. Gangireddy, M. Komarasamy, E.J. Faierson, R.S. Mishra, High strain rate mechanical behavior of Ti-6Al-4V octet lattice structures additively manufactured by selective laser melting (SLM), Materials Science and Engineering: A 745 (2019) 231-239.
[113] M.J. Donachie, Titanium: a technical guide, ASM international2000.
[114] S. Gangireddy, Effect of Initial Microstructure on High-Temperature Dynamic Deformation of Ti-6Al-4V Alloy, Metallurgical and Materials Transactions A 49(10) (2018) 4581-4594.
[115] P. Koehnen, C. Haase, J. Bueltmann, S. Ziegler, J.H. Schleifenbaum, W. Bleck, Mechanical properties and deformation behavior of additively manufactured lattice structures of stainless steel, Materials & Design 145 (2018) 205-217.

[116] K. Kempen, L. Thijs, E. Yasa, M. Badrossamay, W. Verheecke, J. Kruth, Process optimization and microstructural analysis for selective laser melting of AlSi10Mg, Solid Freeform Fabrication Symposium, 2011, pp. 484-495.
[117] S. Das, Physical aspects of process control in selective laser sintering of metals, Advanced Engineering Materials 5(10) (2003) 701-711.
[118] P. Kobryn, S. Semiatin, Mechanical properties of laser-deposited Ti-6Al-4V, Solid freeform fabrication proceedings, Austin, 2001, pp. 6-8.
[119] H. Von Schnering, R. Nesper, Nodal surfaces of Fourier series: fundamental invariants of structured matter, Zeitschrift für Physik B Condensed Matter 83(3) (1991) 407-412.
[120] https://cdn0.scrvt.com/eos/ff2fe7fc83afe675/fd457bd16965/NiAll-HX-M290-400W_Material_data_sheet_10-15_en.pdf, Material Data sheet.).
[121] https://www.directindustry.com/prod/allied-high-tech-products/product-34997-1137575.html).